Control of a Rigid Wing Pumping Airborne Wind Energy System in all Operational Phases

Davide Todeschini[a], Lorenzo Fagiano[a,*], Claudio Micheli[b], Aldo Cattano[c]

[a]*Dipartimento di Elettronica, Informazione e Bioingegneria, Politecnico di Milano*
Piazza Leonardo da Vinci 32, 20133 Milano, Italy
[b]*Auterion Inc., Edenstrasse 20, 8045 Zürich, Switzerland*
[c]*Skypull SA, Via alla Stampa 49, 6967 Lugano, Switzerland*

Abstract

The control design of an airborne wind energy system with rigid aircraft, vertical take-off and landing, and pumping operation is described. A hierarchical control structure is implemented, in order to address all operational phases: take-off, transition to power generation, pumping energy generation cycles, transition to hovering, and landing. Control design at all hierarchical levels is described. The design approach is conceived and developed with real-world applicability as main driver. Aircraft design considerations in light of system maneuverability are presented, too, as well as three possible alternative strategies for the retraction phase of the pumping cycle. The automatic control approach is assessed in simulation with a realistic model of the overall system, and the results yield a comparison among the three retraction strategies, clearly indicating the most efficient one. The presented results allow one to simulate the dynamical behavior of an AWE system in all operational phases, enabling further studies on all-round system automation, towards fully autonomous and reliable operation.

Keywords: Airborne Wind Energy, Nonlinear control, Hierarchical control, Aircraft control, Wind energy

---

*Corresponding author
   Email address:* `lorenzo.fagiano@polimi.it` (Lorenzo Fagiano)

1. Introduction

An Airborne Wind Energy (AWE) system converts wind energy into electricity or traction power (e.g., for naval propulsion) with an autonomous tethered aircraft that carries out periodic trajectories in the wind flow [1, 2]. Deemed a potential game-changing solution [3], AWE is attracting the attention of researchers, entrepreneurs, and policy makers alike [4, 5], with the promise of producing large amounts of cost-competitive electricity and with wide applicability worldwide [6, 7, 8, 9]. Today, AWE is the umbrella name for a series of technologies under development, which can be classified according to different criteria, such as the operating principle (drag power or pumping operation), aircraft type (rigid or flexible), or take-off and landing method (vertical or linear), see, e.g., [2, 4] for an overview and [10, 11, 12, 13, 14, 15, 16, 17, 18, 19, 20, 21, 22, 23, 24] for contributions on specific aspects.

No fully autonomous AWE system has been commercialized so far: many groups in industry and academia are working to develop the technologies. Fully autonomous and reliable operation is currently one of the major research and development priorities [4]. An essential component to reach this goal is the automatic control system that shall operate the aircraft and the ground station in all the different system and environment conditions, and in all the phases: take-off, power generation, and landing. Such a control system features a hierarchical topology, with control functions at different layers distributed across the various subsystems. In the scientific literature, most contributions focus on control design for the power generation phase, mainly with flexible wings (see, e.g., [12, 13, 16]) but also with rigid ones, [25, 15, 24]. A few works deal with the control aspects of the take-off and/or landing phases [26, 27, 20]. To the best of the authors' knowledge, no contribution so far has described the control of an AWE system in *all* operational phases, allowing one to simulate the dynamical system behavior from take-off, to power generation, to landing, including all transition phases, and eventually to implement the control approach on real-world systems.

This paper provides its main contribution in this direction, by describing a design approach for an automatic control logic able to drive an AWE system in all operational phases. The considered concept employs a rigid aircraft with vertical take-off and landing (VTOL) capability, single tether, and pumping operation, in particular the one with boxed-wing design developed by Skypull SA [28]. Pumping operation entails the repetition of a traction phase, during which the tether is reeled-out under high force, followed by a retraction phase, in which the tether is reeled-in under low force, spending a fraction of the energy generated during traction. We adopt a realistic model of the whole system, and design the feedback controllers at all the hierarchical levels, from the low-level attitude control up to the supervisory state machine that defines the phase transitions, to realize fully autonomous operation in normal (i.e., non-faulty) conditions. In the same spirit as [24], the control system design is approached with simplicity and effectiveness in mind, making it highly suited for implementation on a real prototype. Moreover, this article delivers two additional contributions: 1) a study on the links between aircraft/control design and its maneuverability, exploring the minimum steering radius for a given design as a function of the wind speed, and 2) a comparison among three possible aircraft reentry strategies during the retraction phase of the pumping cycle: a "free-flight" one, where the aircraft glides upwind with very low force on the tether, and two alternatives with taut tether and different flight trajectories. The automatic control system is assessed via numerical simulations, showing the good performance of the approach and allowing us to compare the three reentry alternatives. The comparison clearly confirms that the free-flight strategy achieves the best conversion efficiency, with about 80% ratio between average cycle power and average traction phase power. A preliminary study connected to this paper is [23], where we considered the control in all phases of an untethered aircraft, hence with a simpler model, without the system and control design aspects for tethered flight and power generation, and without the study on different reentry strategies.

The paper is structured as follows. In Section 2, a concise description of the system under study and its operational phases is given. Section 3 presents the

3

analysis of aircraft design vs. maneuverability. Section 4 describes the dynamical system model, divided into its main subsystems: the drone, the tether, and the ground station. Section 5 presents the automatic control strategy. Section 6 describes the simulation results and the comparison among the reentry strategies. Finally, Section 7 contains concluding remarks and points out the next research and development steps.

2. System description and operating principle

We provide next a concise description of the system at hand, while in Section 2.2 we describe its operating principle and the three alternative reentry strategies considered for the retraction phase.

2.1. System description

A sketch of the system considered in this paper is presented in Figure 1. It employs a tethered aircraft with rigid wing (also referred to as "drone" in the remainder) with a single tether and ground-based power conversion via pumping cycle operation. The drone has VTOL capability thanks to onboard propellers. One of the main peculiarities of this system with respect to the other concepts
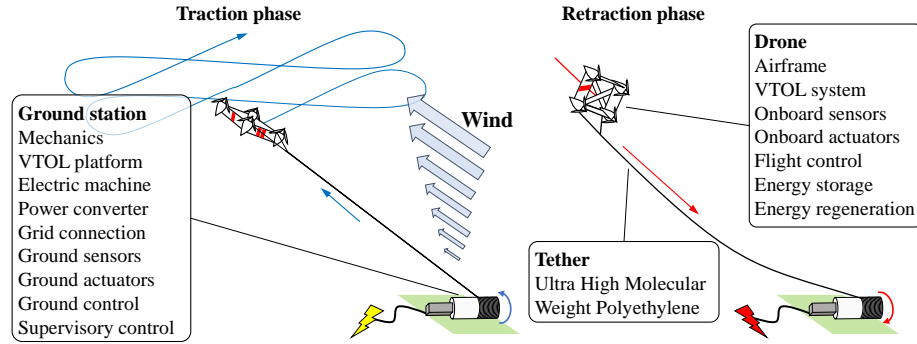

Figure 1: Conceptual sketch of the considered AWE system, with its main components, and of pumping operation.

that are currently under development is the boxed-wing design of the drone with a propeller at each corner, see Figure 2. Due to the distribution of masses
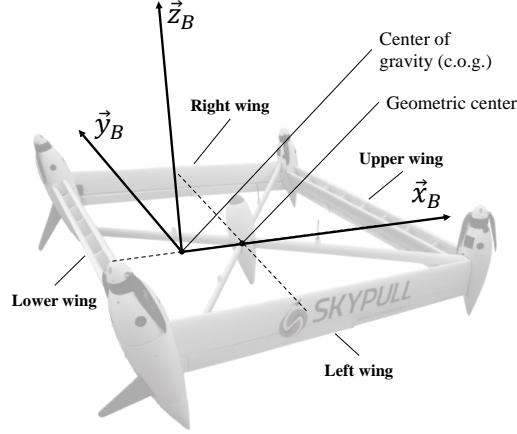
4

Figure 2: Position of the center of gravity and geometric center of the drone, adopted body reference frame B, and indication of upper, lower, left and right wings.

and the positioning of batteries in the lower corners of the frame, the geometric center and the center of gravity are different (see Figure 2). This allows one to identify a lower wing (the one that is closer to the center of gravity) and an upper one (i.e. the opposite one), and consequently a left and right wing by looking at the drone from behind. The tether is attached to the lower part of the drone through a Y-shaped bridle, whose effect is taken into account in the model employed in this study (see Section 4).

On each lateral wing there are two discrete control surfaces, while the upper and lower wings feature three discrete control surfaces each. These surfaces can be actuated either symmetrically, on a single wing or on two opposite wings, leading to a symmetric change of aerodynamic coefficients (hence of lift and drag forces), or in opposite directions. In the second case, the effect is to generate turning moments. All the possible combinations of movements of the control surfaces lead to a rather high control authority when operating in dynamic flight mode. In addition, the four propellers act as in standard quad-copters in hovering mode, and they can further contribute to turning moments also in dynamic flight mode, besides providing the forward thrust to keep cruise velocity. In this report, we assume that the control system can inject turning moments around

5

the axes of the body coordinate system $B = (\vec{x}_B, \vec{y}_B, \vec{z}_B)$ depicted in Figure 2, plus a thrust force in the $\vec{z}_B$ direction. Therefore, we have four control inputs (three turning moments and the thrust force). The translation from turning moments to individual surface/propeller commands is managed by a low-level logic that aims to provide the wanted action with minimal energy consumption. When operating in tethered mode in presence of strong-enough wind, the propellers are not used to generate thrust force, rather the forward apparent speed is provided by the well-known phenomena of crosswind kite power [29],[30]. Regarding the tether, this is made of Ultra-High Molecular Weight Polyethylene (UHMWPE), as in most pumping AWE systems. Finally, the ground station features a winch connected to an electric machine that serves both as generator and as motor during pumping operation, together with all the required subsystems (power electronics, energy storage, mechanical frame, tether spooling system, ground control system, ground sensors, etc.).

2.2. Operating principle and reentry strategies

In normal (i.e. non-faulty) conditions, the working principle of this class of system features the following phases:

- **Vertical take-off**. When the wind conditions at the target operating altitude are suitable to generate energy (cut-in wind speed), the system takes-off vertically using the on-board propellers, in hovering mode. This is the typical flight condition of quad-rotors, with the addition of the tether. The propellers sustain the weight of the vehicle and control its attitude.

- **Transition from hovering to power generation**. In this phase, the drone must quickly speed up and rotate to achieve the attitude and reference speed that can sustain its weight during the power generation phase.

- **Power generation**. The system transitions from multi-copter mode to dynamic flight and enters into power generation mode. This is achieved via the so-called "pumping operation", composed of two phases (see Figure 1):

6

in the traction phase the drone flies fast in crosswind patterns (i.e. roughly perpendicular to the wind flow), like a steerable kite, and the tether is reeled-out under high force, generating energy, while in the retraction phase the drone glides towards the ground station and the tether is quickly reeled-in under very low force, spending a fraction of the energy previously generated. Two transition phases link the traction and retraction ones to achieve a repetitive power generation cycle. During power generation, the aircraft is kept airborne by large aerodynamic forces, the onboard propellers are therefore not employed, or they are used as generators to recharge the batteries and supply power to the onboard electronics and actuators. This is the typical flight condition of an airplane, with the addition of the tether.

- **Transition from flight to hovering**. In this phase, the drone must slow down and rotate with propellers pointing up, to achieve a stationary hovering condition.

- **Vertical landing**. When the wind is too weak to generate energy, or too strong to operate the system safely, the drone carries out a controlled vertical landing in hovering mode.

The main control objective is to obtain a fully autonomous flight cycle from take-off to landing, going through all the phases described above.

The model and control algorithms presented in this paper allow one to realize such an all-round operation.

2.2.1. Alternative reentry strategies

The efficiency of the pumping cycle depends on how the traction and retraction phases are carried out. While for the traction phase there is clear consensus in the literature and among AWE developers on the type of trajectory that must be flown (crosswind patterns, either loops or figures of eight), for the retraction phase there are several options that can be explored for what we call the *reentry* strategy. The latter term refers to the way the aircraft is flown to a suitable

condition to start the next traction phase, while the ground station reels-in the tether. One of the contributions of this paper is indeed to compare three different alternative reentry strategies and their effect on the cycle performance in terms of average power generation. It is appropriate to describe qualitatively these three alternative strategies at this point, while in Section 5 we will point out the corresponding specific control solutions. In the remainder, we adopt the term "free-flight" to indicate a flight mode with slack tether, as opposed to "taut-tether" flight. To visually present the three alternatives, we anticipate in Figures 3-5 part of the simulation results presented in Section 6.

Free-flight reentry. With this strategy, the reentry starts with the drone transitioning from taut-tether flight into free-flight. The ground station controller regulates the tether speed in order to limit the pulling force at very small values, thus limiting interference with the drone control system that regulates the drone's trajectory in a free-flight condition. Then, the drone starts to glide upwind towards the ground station at controlled speed. To facilitate the restart of the next traction phase, in which the drone enters a figure-of-eight path, the gliding trajectory is carried out pointing to one side of the ground station with respect to the wind direction. When the drone is sufficiently close to the ground station, its control system cooperates with the ground station's one in order to transition again from free-flight to tethered flight. This is the most critical part of the trajectory and requires very accurate coordination of on-board and on-ground controllers, to avoid tether force peaks that could significantly perturb the trajectory of the drone or even damage the latter. Figure 3 presents a pumping cycle obtained with the free-flight reentry.

Complete rotation around the ground station. The second alternative consists in a complete revolution of the aircraft around the ground station, while the tether is reeled-in at constant speed. The drone thus flies a spiraling trajectory. In this case, the tether is maintained taut at all times. To maximize the cycle efficiency, the reference tether velocity has to be adequately calibrated, in order to avoid large peaks of required power and at the same time guarantee a sufficiently fast tether reel in. This strategy is presented in Figure 4.
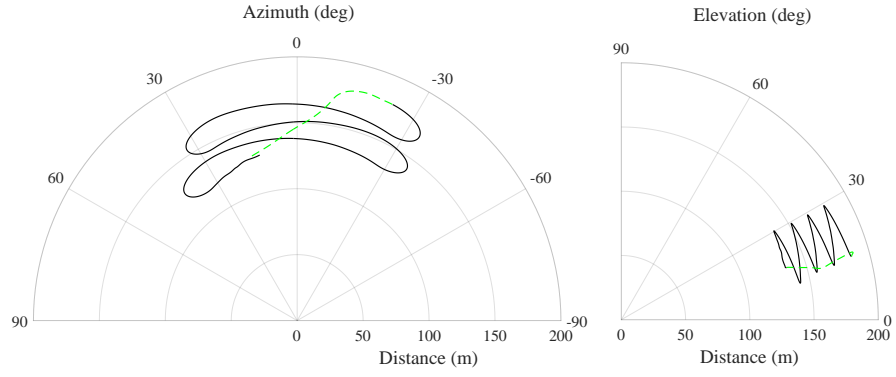
8

Figure 3: Simulation of a pumping cycle with free-flight reentry strategy: drone path in polar coordinates. Black solid line: traction phase; green dashed line: retraction phase.
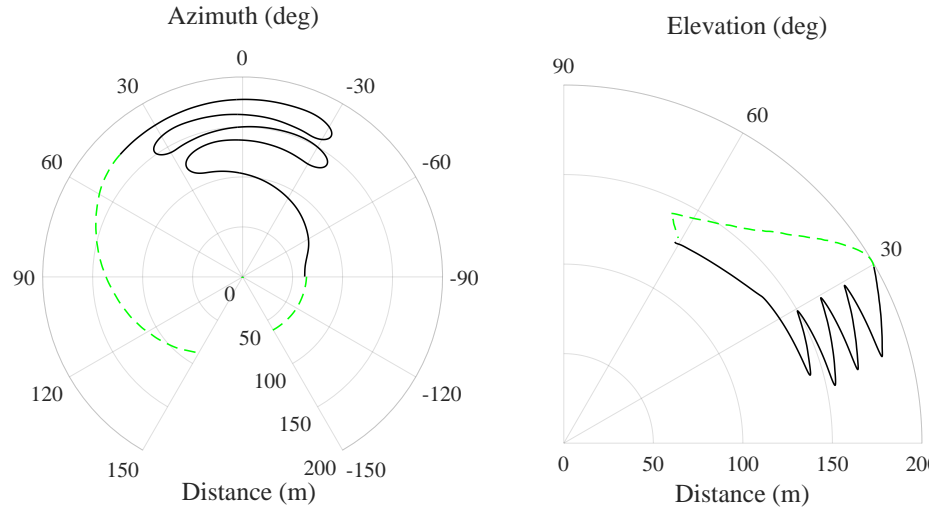

Figure 4: Simulation of a pumping cycle with rotation around the ground station as reentry strategy: drone path in polar coordinates. Black solid line: traction phase; green dashed line: retraction phase.
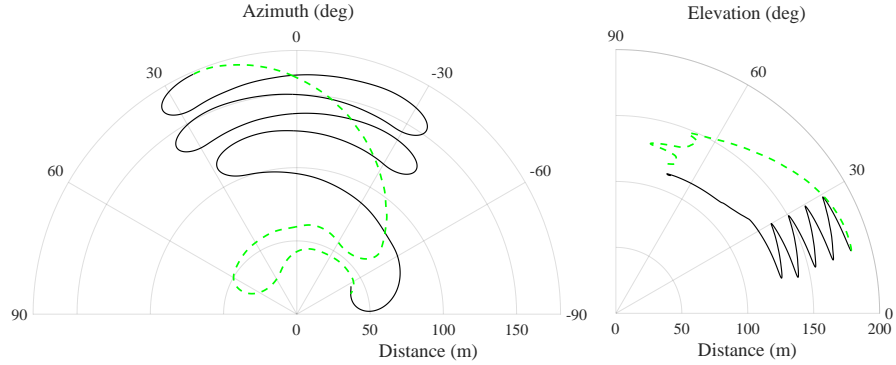
Figure 5: Simulation of a pumping cycle with climb and descend reentry strategy: drone path in polar coordinates. Black solid line: traction phase; green dashed line: retraction phase.

Climb and descend reentry. In this strategy, the drone continues to follow a figure-of-eight path, but at an higher elevation from ground than the one used in the traction phase. In this way, the apparent wind seen by the drone decreases, and the retraction phase is carried out under relatively low tether force. Also in this case, the reference tether velocity has to be suitably calibrated to optimize the cycle performance. Figure 5 depicts the typical trajectory obtained with this strategy.

3. Steering authority analysis and drone design considerations

The steering authority during tethered flight is a crucial aspect for an AWE system, because of the particular trajectories to be achieved. We term steering authority of the tethered system the minimum turning radius that it can achieve while flying with taut tether under high lift force and apparent speed. The smaller such a steering radius, the higher the steering authority. The latter is affected by different aspects, including the steering strategy which, for the considered box-wing design, can be either "roll-based" or "yaw-based". Here, roll and yaw deviations are referred to a reference system, which we formally introduce in Section 4, defined by the drone's position when the tether is taut. In particular, the yaw angle is measured around the tether direction, while the

10

roll angle is measured with respect to a neutral configuration where the upper and lower wings are perpendicular to the tether.

In our research, we went through an initial design phase in which we analyzed these two options. In this section, we present the key points of our analysis, since they motivate subsequent control design choices and they can be useful also for other AWE systems' developments. In particular, we analyze the steering authority in two different conditions: 1) trajectories parallel to ground, and 2) trajectories perpendicular to ground. These are indeed two extreme cases of all the situations that can occur in tethered crosswind flight. In the analysis, we make the following simplifying assumptions:

- the apparent speed magnitude v_a coincides with the drone's velocity vector magnitude (i.e. no absolute wind speed is present), indicated with v in this study. The results hold qualitatively also in presence of wind, particularly in crosswind conditions when the absolute wind speed is much smaller than the aircraft's speed relative to ground;

- the apparent wind velocity is such that the lift force significantly exceeds the aircraft weight: the excess lift is balanced by the tether force (i.e., the cable essentially acts as kinematic constraint preventing the drone from translating in tether's direction);

- the tether direction is perpendicular to the flown path;

- in the roll-based strategy the side-slip angle β of the aircraft is zero.

These assumptions are reasonable for a first-approximation analysis of steering authority. A conceptually similar approach has been used already in the field of AWE, for example to study the steering mechanism of kites, obtaining good matching with the experimental evidence [31, 32].

3.1. Trajectories parallel to ground

The centrifugal force during a turn at constant radius r can be expressed as:

$$F_{cf} = m\frac{v^2}{r} \tag{1}$$

where m is the drone mass and v is its speed. The centrifugal force has to be counterbalanced by a centripetal one in order to turn at constant radius r. The generation mechanism of the centripetal force depends on the considered steering strategy, as described below.

3.1.1. Roll-based steering strategy

With roll-based steering, the centripetal force F_{cp} is given by:

$$F_{cp} = (F_{L,up} + F_{L,down})\sin(\varphi) \tag{2}$$

where $F_{L,up}$, $F_{L,down}$ are the lift forces contributed by the upper and lower wings and φ is the drone's roll angle, so to obtain the projection of the lift forces on the plane containing the drone's trajectory (see Figure 6). The lift
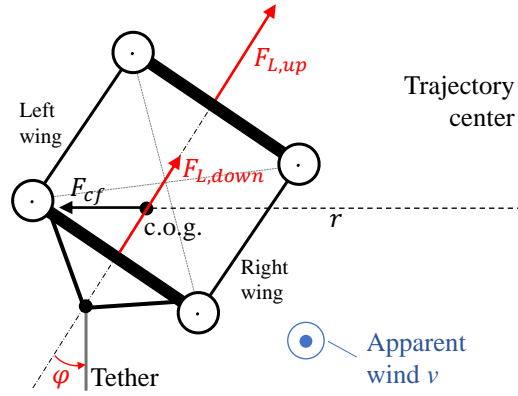

Figure 6: Sketch of turning maneuver using the roll-based strategy.

forces are computed as:

$$
\begin{aligned}
F_{L,up} &= \tfrac{1}{2}\rho S_{up} c_L(\alpha,\beta)v^2 \\
F_{L,down} &= \tfrac{1}{2}\rho S_{down} c_L(\alpha,\beta)v^2
\end{aligned} \tag{3}
$$

12

where ρ is the air density, S_{up}, S_{down} are the effective surfaces of the upper and lower wings, c_L is their lift coefficient, and α, β are the drone's angle of attack and side-slip angle, respectively. The specific aerodynamic coefficients employed in our study are reported in Section 6 (Figure 17).

Equating (1) and (2) and inserting (3) into (2) we have

$$\frac{1}{2}\rho(S_{up} + S_{down})c_L(\alpha, \beta)v^2 \sin(\varphi) = m\frac{v^2}{r} \tag{4}$$

solving for the turning radius and considering that we assume $\beta = 0$, we finally obtain:

$$r = \frac{2m}{\rho(S_{up} + S_{down})c_L(\alpha, 0)\sin(\varphi)} \tag{5}$$

From this equation it can be noted that, to increase the steering authority using a roll-based strategy, one of the following measures can be adopted, compatibly with other design and control requirements:

- Reduce the drone mass m;

- Increase the upper and lower wing surfaces S_{up}, S_{down};

- Increase the lift coefficient c_L (e.g. higher angle of attack α);

- Increase the roll angle φ.

3.1.2. Yaw-based steering strategy

In the yaw-based steering (see Figure 7), the centripetal force is the sum of the lift forces $F_{L,left}$, $F_{L,right}$ of the lateral wings. The latter are non-zero due to the presence of a side-slip angle induced by the yaw motion:

$$
\begin{aligned}
F_{L,left} &= \tfrac{1}{2}\rho\, S_{left}\, c_{L,lateral}(\beta)v^2 \\
F_{L,right} &= \tfrac{1}{2}\rho\, S_{right}\, c_{L,lateral}(\beta)v^2 \\
F_{cp} &= F_{L,left} + F_{L,right}
\end{aligned}
\tag{6}
$$

where S_{right}, S_{left} are, respectively, the surface of the left and right wings, and $c_{L,lateral}(\beta)$ their lift coefficient. The latter is a function of the side-slip angle β, which for the lateral wings corresponds to the angle of attack. In this case,
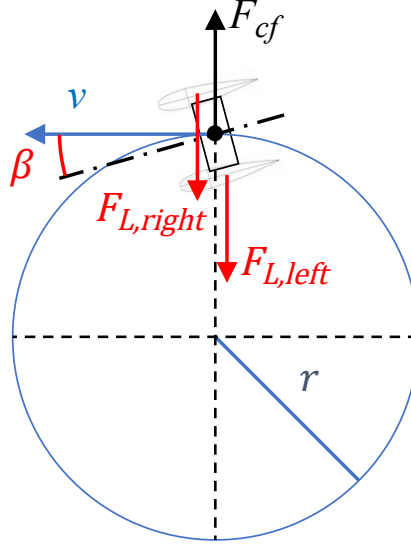
13

Figure 7: Sketch of turning maneuver using the yaw-based strategy.

the force balance $F_{cp} = F_{cf}$ yields:

$$\tfrac{1}{2}\rho(S_{left} + S_{right})c_{L,lateral}(\beta)v^2 = m\tfrac{v^2}{r} \tag{7}$$

The turning radius is given by:

$$r = \frac{2m}{\rho(S_{left} + S_{right})c_{L,lateral}(\beta)} \tag{8}$$

Thus, to increase the steering authority with a yaw-based strategy, one of the following measures can be adopted:

- Reduce the drone mass m;

- Increase the lateral wings' surfaces S_{left}, S_{right};

- Increase the lift coefficient of the lateral wings, $c_{L,lateral}$;

- Increase the side slip angle β (without exceeding its limits for a stable flight).
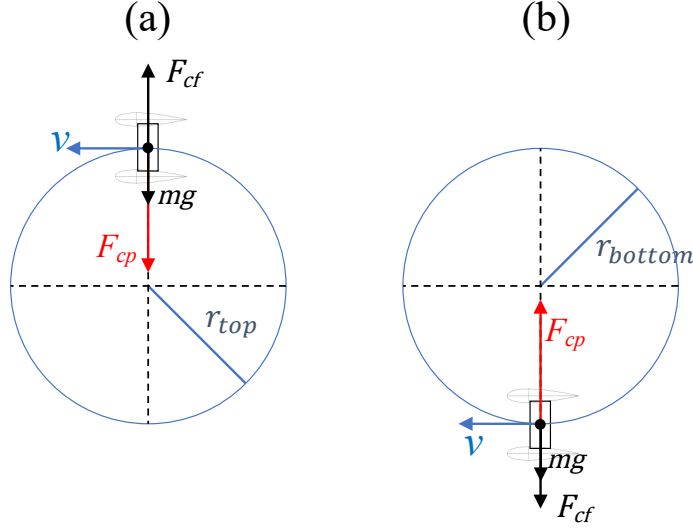
14

Figure 8: Sketch of turning maneuver with path perpendicular to ground: top of trajectory (a) and bottom of trajectory (b).

3.2. Trajectories perpendicular to ground

In the previous section, results for trajectories parallel to ground (i.e. with the gravity force roughly in tether direction and compensated by the lift) have been presented. However, in crosswind flight with low elevation, the flown tra-
jectories tend to be perpendicular to the ground, so that the steering authority is affected also by the gravity force mg (where g is the gravity acceleration), which is roughly perpendicular to the tether direction. Moreover, the effect of gravity depends on the specific position on the flown path. Considering for simplicity a loop, the gravity force contributes to the centripetal force when the
curvature is downwards (i.e. at the top of the trajectory), while it adds to the centrifugal force when the curvature is upwards (at the bottom of the trajec-
tory). Thus, during trajectories not parallel to ground, the steering authority is bounded between two extremes, as described below.

15

Table 1: Parameters used for the steering authority analysis of Figure 9

Parameter	Unit	Value
S_{up}, S_{down}	m^2	0.21
S_{left}, S_{right}	m^2	0.21
$c_L(\alpha, 0)$	-	1
$c_{L,lateral}(\beta)$	-	1
m	kg	11
ρ	kg/m^3	1.2
g	m/s^2	9.81

3.2.1. Top of trajectory

Referring to Figure 8-(a), we have:

$$F_{cf} = F_{cp} + mg \tag{9}$$

where F_{cp} is provided by either one of the two strategies presented in the previous section (i.e. equation (2) or (6)). Solving for the turning radius we obtain:

$$r_{top} = \frac{mv^2}{F_{cp} + mg} \tag{10}$$

From (10) it can be noted that, in the upper part of the trajectory, the gravity force is a centripetal one, helping the drone to turn. The behavior of r_{top} as a function of the apparent speed is best analyzed graphically, by computing it for increasing speed values. We present an example in Figure 9, obtained with a yaw-based strategy and using the parameters reported in Table 1. Note that r_{top} increases with speed and asymptotically approaches a value r which corresponds to the one found for trajectories parallel to ground. This is reasonable, since the gravity force becomes negligible with respect to the aerodynamic forces at high apparent speed, as assumed in the popular first-principle analysis of AWE generation potential [29].
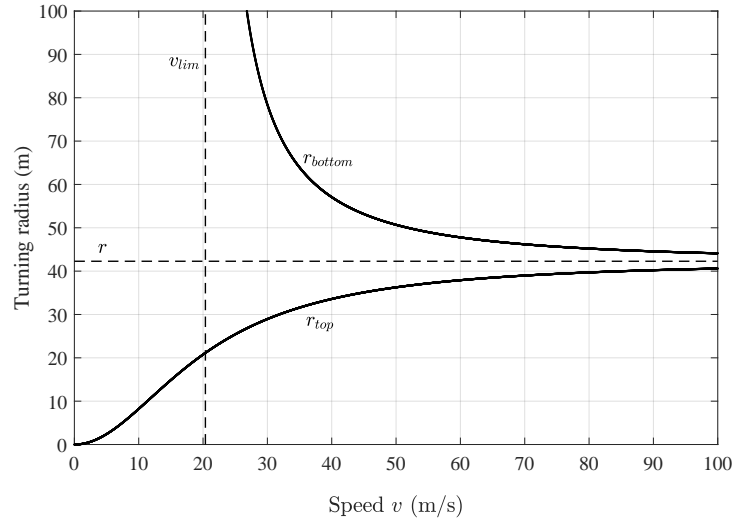
16

Figure 9: Example of relation between turning radius and front speed for a path perpendicular to ground, for the Skypull system considered in this study and using a yaw-based strategy. The turning radius at the upper part of the trajectory, r_{top}, (10) and at the bottom, r_{bottom} (12), are shown together with the asymptotic value r (8) and the limiting speed v_{lim}. Drone parameters reported in Table 1.

3.2.2. Bottom of trajectory

Referring now to Figure 8-(b), we have:

$$F_{cf} = F_{cp} - mg \tag{11}$$

and solving for the turning radius we obtain

$$r_{bottom} = \frac{mv^2}{F_{cp} - mg} \tag{12}$$

from which it can be noted that in this case gravity provides a centrifugal contribution, reducing the steering authority. Equation (12) has a singularity at a value of speed v_{lim} such that the centripetal forces generated by the wings (be it with roll-based or yaw-based strategies) is equal to the gravity force: below this speed, the drone is not able to steer in the lower part of trajectory, because the available centripetal force is not large enough to compensate the weight. This also corresponds to the minimum airspeed to keep the drone airborne. Computing the value of r_{bottom} with increasing speed reveals that the turning radius decreases with larger speed values and approaches the same asymptotic value r, see Figure 9.

3.3. Conclusions

From the presented analysis, the following considerations emerge:

- During trajectories perpendicular to ground, the turning radius is bounded in the inteval $[r_{top}, r_{bottom}]$;

- For trajectories parallel to ground, as a first approximation the front speed does not affect the steering authority. Instead, for trajectories perpendicular to ground, the steering authority is highly affected by speed and it approaches a unique asymptotic value with larger speed, either from above (in the top part of the trajectory) or from below (in the bottom part), see Figure 9.

- In a drone with lower mass, higher lift, or larger effective surface area, the singularity point v_{lim} and the asymptotic radius r are shifted to lower values, with an increase of the steering authority.
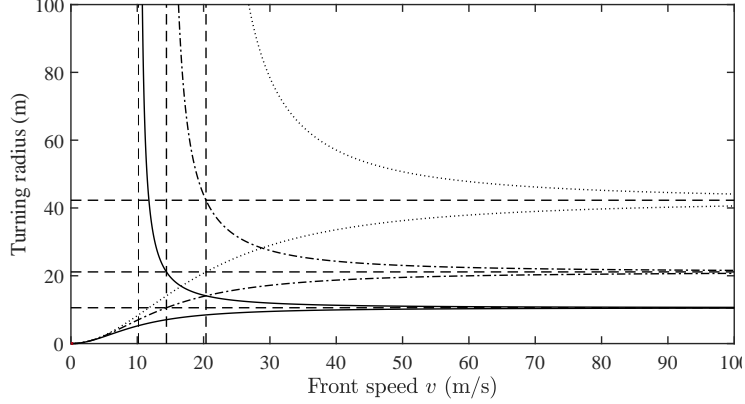
18

Figure 10: Turning radii of the Skypull system considered in this study as a function of front speed, for the baseline total lateral surface (dotted line), and for increased surface values: twice the baseline (dash-dotted), and four times the baseline (solid). Drone parameters reported in Table 1.

Regarding the last point above, Figure 10 shows the sensitivity of the turning radius with respect to the effective lateral wings' surface in a yaw-based strategy, keeping constant all other parameters. A larger surface decreases the turning radius in all conditions and reduces the minimum front speed required to steer at the bottom part of the path. From this analysis, it can be noted that doubling the lateral surfaces has a large impact on the steering authority, while further doubling it has a relatively lower effect, since the relationship is hyperbolic (see, e.g., (8)). Moreover, this simplified analysis is not valid anymore for small radius values (as compared with the drone's wingspan), since it does not take into account that when the turn is too narrow the lift distribution along the wing becomes highly uneven, and the total lift decreases significantly.

Based on the presented analysis, in our research we eventually decided to adopt a yaw-based strategy and to double the lateral wing surfaces with respect to the original drone design, in order to improve maneuverability. The choice of yaw-based strategy was also influenced by the fact that the considered system

19

features a tether attachment point significantly below the center of gravity, which leads to a self-aligning roll moment when the tether pulls the aircraft, making it more difficult to issue the roll deviations required for steering. This aspect is further analyzed in Section 4.2.

4. System model

In this section, we describe the dynamic models of the drone and of the ground station that we use to simulate the system. For the control design, described in Section 5, we use different, simplified models. In this way, we also introduce a realistic mismatch between the model used for control design and the one used to simulate the system and evaluate the control performance. For the sake of notational simplicity, in the remainder we omit the explicit dependency of the various quantities on the continuous-time variable $t \in \mathbb{R}$, when this is clear from the context. Finally, the symbol $\cdot^T$ denotes the matrix transpose operation.

4.1. Reference frames

The considered model is derived from established 6-dof aircraft model equations [33], with modifications due to the box-wing architecture of the drone and the presence of the four propellers.

We start by introducing the drone's position $\vec{p}_{(F)} = [p_{\vec{x}_F}, p_{\vec{y}_F}, p_{\vec{z}_F}]^T$ in the inertial reference frame F $(\vec{x}_F, \vec{y}_F, \vec{z}_F)$, which is centered at the ground station, with unit vector $\vec{z}_F$ pointing up and $\vec{x}_F$ along a chosen direction, here assumed to coincide with the prevalent wind direction at the considered location. For taut-tether control purposes, it is useful to convert the coordinates of the inertial system into spherical ones:

$$
\begin{bmatrix} d \\ \theta_{el} \\ \varphi_{az} \end{bmatrix} = \begin{bmatrix} \sqrt{p_{\vec{x}_F}^2 + p_{\vec{y}_F}^2 + p_{\vec{z}_F}^2} \\ \arctan\left(\frac{p_{\vec{z}_F}}{\sqrt{p_{\vec{x}_F}^2 + p_{\vec{y}_F}^2}} \right) \\ \arctan2\left(p_{\vec{x}_F}, p_{\vec{y}_F} \right) \end{bmatrix}
\tag{13}
$$

20

where d is the drone distance from ground station, θ_{el} is the elevation angle and φ_{az} is the azimuth angle (Figure 11, left), and $\arctan2(\cdot, \cdot)$ is the four-quadrant arctangent function.

For convenience when describing the model and the control approach, we introduce three additional right-handed reference frames:

- B $(\vec{x}_B, \vec{y}_B, \vec{z}_B)$ is the body reference frame, fixed to the drone and with origin in its center of gravity (Figure 2). The $\vec{z}_B$ axis is aligned with propellers' axes, while $\vec{x}_B$ points towards the upper wing. The $\vec{z}_B$ axis of this reference system is thus aligned with the $\vec{z}_F$ axis of the inertial one when the UAV is stationary in hovering mode.

- A_w $(\vec{x}_{A_w}, \vec{y}_{A_w}, \vec{z}_{A_w})$ is the apparent wind reference system, with $\vec{x}_{A_w}$ aligned with the apparent wind direction, $\vec{y}_{A_w}$ parallel to the upper wing, and $\vec{z}_{A_w}$ pointing up.

- L $(\vec{L}_T, \vec{L}_N, \vec{L}_W)$ is the local (or tether) reference frame, fixed to the UAV and with $\vec{L}_T$ aligned with tether, pointing opposite to the ground station, $\vec{L}_N$ pointing to the local North and $\vec{L}_W$ pointing to local West (see Figure 11, left).

The relative orientation between frames F and B can be expressed by a quaternion $\vec{q} = \begin{bmatrix} q_1 & q_2 & q_3 & q_4 \end{bmatrix}^T$.

A vector given in the F system can be expressed in the B system by means of the following rotation matrix:

$$H_{FB} = 2 \begin{bmatrix} (q_1^2 + q_2^2) - 1 & (q_2 q_3 + q_1 q_4) & (q_2 q_4 - q_1 q_3) \\ (q_2 q_3 - q_1 q_4) & (q_1^2 + q_3^2) - 1 & (q_3 q_4 + q_1 q_2) \\ (q_2 q_4 + q_1 q_3) & (q_3 q_4 - q_1 q_2) & (q_1^2 + q_4^2) - 1] \end{bmatrix}, \qquad (14)$$

and vice-versa a vector in B system can be translated into F system by matrix $H_{BF} = H_{FB}^T$. A vector expressed in A_w reference can be expressed in B system
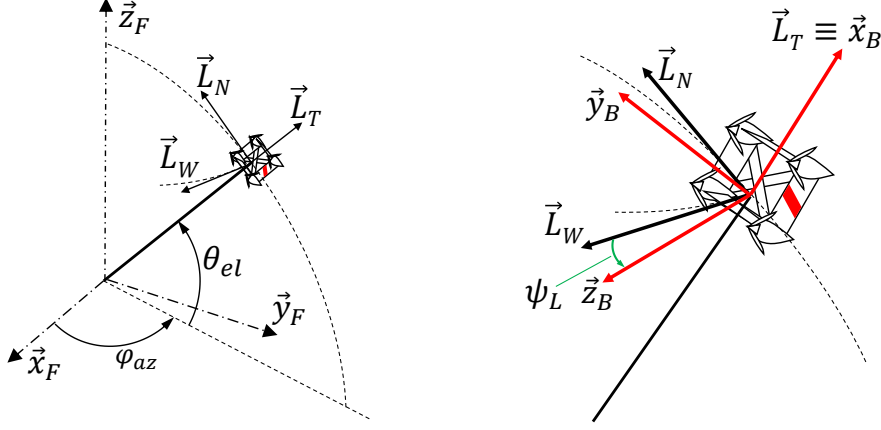
21

Figure 11: Left: spherical coordinates. The drone position can be expressed in terms of distance from ground station, elevation angle θ_{el}, and azimuth angle φ_{az}. A sketch of the local reference system L is presented as well: L_T is directed along the tether, L_N points to the local North (zenith) and L_W points the local West. Right: close-up view of the local reference system, and Euler angle ψ_L.

by the following rotation matrix [33]:

$$
H_{WB} = \begin{bmatrix} \cos(\alpha) & 0 & -\sin(\alpha) \\ \sin(\alpha)\sin(\beta) & \cos(\beta) & \cos(\alpha)\sin(\beta) \\ \sin(\alpha)\cos(\beta) & -\sin(\beta) & \cos(\alpha)\cos(\beta) \end{bmatrix} \tag{15}
$$

where, as already introduced in Section 3, α is the drone's angle of attack and β is the side-slip angle. Finally, the rotation matrix from F to L reads:

$$
H_{FL} = \begin{bmatrix} \cos(\theta_{el})\cos(\varphi_{az}) & \cos(\theta_{el})\sin(\varphi_{az}) & \sin(\theta_{el}) \\ -\sin(\theta_{el})\cos(\varphi_{az}) & \sin(\theta_{el})\sin(\varphi_{az}) & \cos(\theta_{el}) \\ \sin(\varphi_{az}) & -\cos(\varphi_{az}) & 0 \end{bmatrix} \tag{16}
$$

4.2. Drone model

Due to the unbalance in mass distribution mentioned in Section 2, the constant inertia matrix computed with respect to the B frame has non-zero terms

out of the diagonal:

$$I = \begin{bmatrix} I_{xx} & 0 & I_{zx} \\ 0 & I_{yy} & 0 \\ I_{zx} & 0 & I_{zz} \end{bmatrix} \tag{17}$$

The external forces and moments acting on the UAV considered in the model are:

- Gravitational force;

- Propellers' forces and moments;

- Aerodynamic force and moments;

- Tether force and moments.

The gravitational force is computed in the inertial frame as $\vec{F}_{g(F)} = m \begin{bmatrix} 0 & 0 & -g \end{bmatrix}^T$, where the constants m and g are, respectively, the drone's mass and the gravity acceleration.

Each propeller generates a thrust force, $\vec{F}_{p(B)j}$, and a drag torque in $\vec{z}_B$ direction, $T_{p(B)j}$, $j = 1 \dots, 4$, expressed in body frame as:

$$\begin{aligned} \vec{F}_{p(B)j} &= \begin{bmatrix} 0 & 0 & b_j \omega_j^2 \end{bmatrix}^T \\ \vec{T}_{p(B)j} &= \begin{bmatrix} 0 & 0 & c_j \omega_j^2 \end{bmatrix}^T \end{aligned} \tag{18}$$

Where ω_j is the rotational speed the jth propeller, and b_j, c_j are constant parameters. The propellers' forces can be linearly combined to obtain the total thrust in $\vec{z}_B$ direction, denoted by U_1, and the rotational moments around $\vec{x}_B$ (ΔU_{p2}), $\vec{y}_B$ (ΔU_{p3}) and $\vec{z}_B$ (ΔU_{p4}):

$$\begin{bmatrix} U_1 \\ \Delta U_{p2} \\ \Delta U_{p3} \\ \Delta U_{p4} \end{bmatrix} = \begin{bmatrix} b_1 & b_2 & b_3 & b_4 \\ b_1 d_{\vec{y}_B 1} & -b_2 d_{\vec{y}_B 2} & -b_3 d_{\vec{y}_B 3} & b_4 d_{\vec{y}_B 4} \\ b_1 d_{\vec{x}_B 1} & -b_2 d_{\vec{x}_B 2} & b_3 d_{\vec{x}_B 3} & -b_4 d_{\vec{x}_B 4} \\ -c_1 & -c_2 & c_3 & c_4 \end{bmatrix} \begin{bmatrix} \omega_1^2 \\ \omega_2^2 \\ \omega_3^2 \\ \omega_4^2 \end{bmatrix} \tag{19}$$

where $d_{\vec{x}_B i}$, $d_{\vec{y}_B i}$, $i = 1, \dots, 4$ are the constant position coordinates of each propeller with respect to the origin of B.

23

When deriving the model of the drone's aerodynamics, we took into account the various application points of the aerodynamic force and moment vectors generated by the four wings. Moreover, the angle of attack of one wing corresponds to the side-slip angle for the perpendicular one, thus resulting in a rather complex computation of the forces and moments acting at each instant on the drone. As a matter of fact, the overall aerodynamic force and moment vectors are nonlinear mappings whose inputs are the drone's angle of attack and side-slip, the apparent wind speed vector, and the actuators' position. In the apparent wind reference system (A_w), the aerodynamic force vector can be expressed as:

$$\vec{F}_{aero(A_w)} = \begin{bmatrix} F_D & F_S & F_L \end{bmatrix}^T. \tag{20}$$

F_D, F_S, F_L are the drag component, lateral component, and lift component, respectively, computed as:

$$\begin{aligned} F_L &= \tfrac{1}{2}\rho S c_{L,tot}(\alpha,\beta) v_a^2 \\ F_D &= \tfrac{1}{2}\rho S c_{D,tot}(\alpha,\beta) v_a^2 \\ F_S &= \tfrac{1}{2}\rho S c_{S,tot}(\alpha,\beta) v_a^2 \end{aligned} \tag{21}$$

where ρ is the air density, S is the total effective wing area (both constant parameters), v_a is the magnitude of the apparent wind seen by the drone, $c_{L,tot}$, $c_{D,tot}$ and $c_{S,tot}$ are, respectively, the overall lift, drag, and side force coefficients, which are functions of (α, β). These lumped parameters take into account the specific geometry of the drone and of the airfoils employed on each one of the four wings. In this study, which is focused on control aspects, we neglect the damping terms in the computation of aerodynamic forces and moments. We think that this is an acceptable simplification here, since the aircraft is stabilized anyways by active control and we expect that the presence of these terms would not affect significantly the results. Similarly, the overall aerodynamic moment vector, denoted with $\vec{M}_{aero}$, is computed in frame A_w as a quadratic function of v_a and a nonlinear function of (α, β), featuring suitable constant aerodynamic coefficients. In particular, a CFD analysis was carried out by Skypull to derive the aerodynamic coefficients employed in our model. The employed CFD soft-

ware was SU2 [34], developed by Stanford University. The CFD software results have been validated against experimental data on standard profiles. Moreover, the considered Skypull system has non-planar wings with multi-element airfoils, and the employed software is able to handle these features. As an example, the obtained lift and drag coefficients used in our simulations are presented in Section 6 (Figure 17).

The apparent wind vector $\vec{v}_a$ in the inertial frame is:

$$\vec{v}_{a(F)} = \vec{v}_{w(F)} - \begin{bmatrix} \dot{p}_{\vec{x}_F} \\ \dot{p}_{\vec{y}_F} \\ \dot{p}_{\vec{z}_F} \end{bmatrix} \tag{22}$$

where $\vec{v}_{w(F)}$ is the absolute wind vector.

Regarding the tether, its connection point to the drone is located on a rigid frame attached below the box-wing aircraft (see Figure 12). So, the pulling force also produces a turning moment on the drone. By computing the forces with respect to the body reference frame, we have:

$$\vec{F}_{t(B)} = -\vec{d}_{t(B)}|\vec{F}_t| \tag{23}$$

where $d_{t(B)}$ is the tether direction, computed as (assuming taut tether):

$$\vec{d}_{t(B)} = H_{FB} \frac{\vec{p}_{(F)}}{|\vec{p}_{(F)}|}. \tag{24}$$

The moment generated by the tether force is:

$$\vec{M}_{t(B)} = \vec{p}_{t(B)} \times \vec{F}_{t(B)} \tag{25}$$

where $\vec{p}_{t(B)}$ is the position of the connection point in body reference frame, relative to the center of gravity of the drone (see Figure 12), and $\times$ denotes the cross product. The force magnitude $|\vec{F}_t|$ is computed considering non-zero load transfer only with taut tether:

$$|\vec{F}_t| = \max\left(0, k_s(L_t)(d - L_t)\right) \tag{26}$$

where k_s is the tether stiffness and $(d - L_t)$ is the tether elongation. Tether stiffness is a parameter that depends on the length of reeled-out tether:

$$k_s(L_t) = \frac{F_{t,max}}{\Delta L_{max}} = \frac{F_{t,max}}{\epsilon_{max} L_t} \tag{27}$$
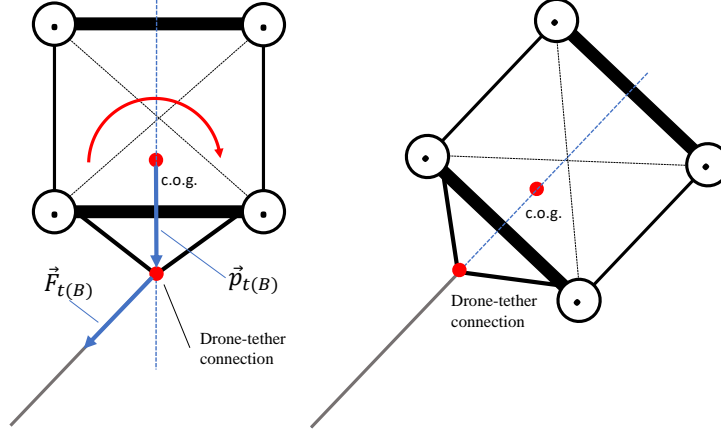
Figure 12: Sketch of the tether connection. The tether force $\vec{F}_{t(B)}$ applies also a moment around the drone's center of gravity.

where $F_{t,max}$ is the maximum force that the tether can withstand, ΔL_{max} is the corresponding maximum elongation, and ϵ_{max} is the maximum elongation relative to the length. Being $\frac{F_{t,max}}{\epsilon_{max}}$ a constant parameter for a given tether, the stiffness depends only on its length, and decreases with it according to the hyperbolic equation (27).

To avoid numerical solution problems, in numerical integration routines it is advisable to implement an approximated version of (26):

$$|\vec{F}_t| = \begin{cases} \frac{F_{t,max}}{\epsilon_{max}}\epsilon, & \text{if } \epsilon \geq \epsilon_0 \\ \frac{F_{t,max}\epsilon_0}{\epsilon_{max}e}e^{\frac{\epsilon}{\epsilon_0}}, & \text{if } \epsilon < \epsilon_0 \end{cases} \tag{28}$$

This formulation is actually identical to (27) for positive elongation, and uses a decreasing exponential approximation for negative elongation. This allows one to avoid the non-differentiable point at zero elongation, which is instead present in (26). The resulting curve is shown in Figure 13. Finally, tether drag is accounted for as an incremental term that increases the drone's aerodynamic drag:

$$c_{D,eq}(\alpha, \beta) = c_{D,tot}(\alpha, \beta) + \frac{c_{D,t}d_t L_t}{8S} \tag{29}$$

where $c_{D,t}$ is the tether drag coefficient, d_t and L_t are, respectively, the tether
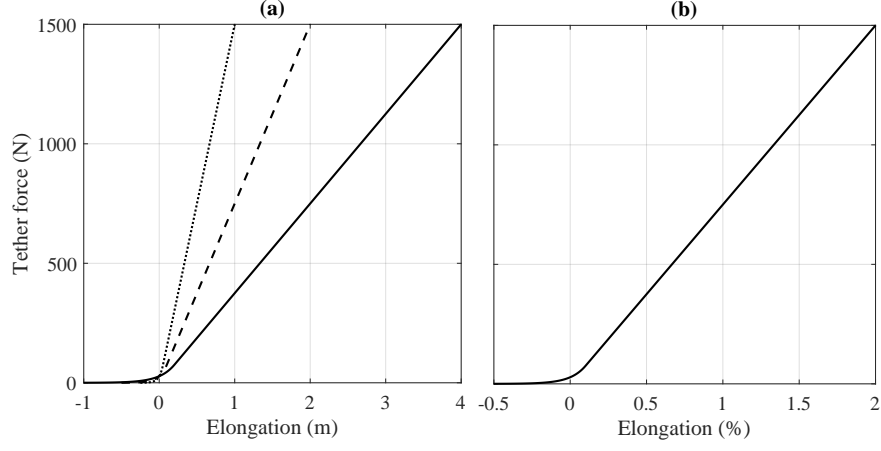
Figure 13: Tether force as a function of (a) absolute elongation and (b) relative elongation, for three different tether length values: 50 m (dotted line), 100 m (dashed), and 200 m (solid).

diameter and its reeled-out length. Equation (29) is derived from a momentum balance considering a linear dependency of the apparent speed seen by each infinitesimal segment of tether, and the distance of such a segment from the ground station, see, e.g., [35]. The coefficient $c_{D,eq}$ is eventually employed to compute the drag force in (21) instead of $c_{D,tot}(\alpha, \beta)$.

Considering all of the described external forces and moments, the resulting drone

27

model consists of 13 ordinary differential equations (ODEs):

$$
\begin{aligned}
F_{\vec{x}_B} &= m(\dot{U} - RV + QW) \\
F_{\vec{y}_B} &= m(\dot{V} - PW + UR) \\
F_{\vec{z}_B} &= m(\dot{W} - QU + PV) \\
M_{\vec{x}_B} &= \dot{P}I_{xx} - (\dot{R} + PQ)I_{zx} + RQ(I_{zz} - I_{yy}) + Q\sum_{j=1}^{4} h_{z,j} \\
M_{\vec{y}_B} &= \dot{Q}I_{yy} + (R^2 + P^2)I_{zx} + PR(I_{xx} - I_{zz}) - P\sum_{j=1}^{4} h_{z,j} \\
M_{\vec{z}_B} &= \dot{R}I_{zz} - (\dot{P} + QR)I_{zx} + PQ(I_{yy} - I_{xx}) \\
\begin{bmatrix} \dot{q_1} \\ \dot{q_2} \\ \dot{q_3} \\ \dot{q_4} \end{bmatrix} &= \frac{1}{2} \begin{bmatrix} 0 & -P & -Q & -R \\ P & 0 & R & -Q \\ Q & -R & 0 & P \\ R & Q & -P & 0 \end{bmatrix} \begin{bmatrix} q_1 \\ q_2 \\ q_3 \\ q_4 \end{bmatrix} \\
\begin{bmatrix} \dot{p}_{\vec{x}_F} \\ \dot{p}_{\vec{y}_F} \\ \dot{p}_{\vec{z}_F} \end{bmatrix} &= H_{BF} \begin{bmatrix} U \\ V \\ W \end{bmatrix}
\end{aligned}
\tag{30}
$$

where U, V and W are the drone's velocity vector components in the body frame B; P, Q and R are the rotational speeds around the axes of B; $F_{\vec{x}_B}$, $F_{\vec{y}_B}$ and $F_{\vec{z}_B}$ are the components in the B frame of the vector sum of all external forces acting on the UAV; $M_{\vec{x}_B}$, $M_{\vec{y}_B}$ and $M_{\vec{z}_B}$ are the components in the B frame of the vector sum of all external moments applied to the UAV. Finally, the constant parameters $h_{z,j}$, $j = 1, \ldots, 4$ are the moments of inertia of motors/propellers in $\vec{z}_B$ direction. The control inputs are the total thrust force, U_1, and the total moments provided by the propellers and by the aerodynamic control surfaces, denoted as U_2, U_3 and U_4 for rotations around axes $\vec{x}_B$, $\vec{y}_B$,, and $\vec{z}_B$, respectively. These variables do not appear explicitly in (30), since they contribute, respectively, to $F_{\vec{z}_B}$, $M_{\vec{x}_B}$, $M_{\vec{y}_B}$ and $M_{\vec{z}_B}$. In particular, the turning moments U_2, U_3 and U_4 are given by the moments ΔU_{p2}, ΔU_{p3}, ΔU_{p4}, provided by the propellers (see (19)) and exploited mainly in hovering mode, plus the contributions of the aerodynamic surfaces, used prevalently in dynamic flight mode. The latter are modeled here directly in terms of control moments. In practice, such moments are nonlinear functions of the positions of the discrete

28

control surfaces that are present on each wing. The precise characterization of such moments as a function of flight conditions and surface position is a proprietary know-how of Skypull SA, not disclosed here for confidentiality reasons. On the other hand, considering directly the control moments U_2, U_3 and U_4 results in a more general approach that can be applied to other drone types, by inserting the corresponding input mapping between discrete control surface positions and resulting moments.

4.3. Ground station model

From rotational equilibrium, the model of the motor-winch subsystem reads:

$$J\ddot{\lambda} = |\vec{F}_t|r_w - T - \beta_f\dot{\lambda} \tag{31}$$

where J is the total moment of inertia of the winch and the motor, λ is the angular position of the winch, r_w is the winch radius, T is the torque applied by the electric machine to the winch and β_f is the viscous friction coefficient. Note that a positive torque $T > 0$ tends to reel-in the tether. We conclude this section on the ground station by introducing the link between the winch position and the length of reeled-out tether:

$$L_t = r_w\lambda. \tag{32}$$

This equation holds under the assumption, without loss of generality, that $\lambda = 0$ corresponds to the tether being completely reeled-in.

5. Control design

We employed simplified models of the system's behavior to design the various control strategies, which will be recalled in this section. The final control approach has been then tested on the full nonlinear model (13)-(31), which captures quite accurately all the relevant effects occurring in the real system. We start our description from the layout of the overall control logic, presented in Figure 14. A supervisory controller is in charge of monitoring the execution
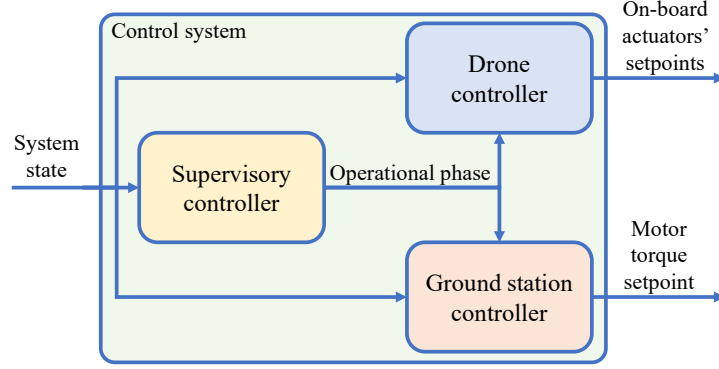
29

Figure 14: Layout of the control system

of the current phase and of switching to the next one. In each phase, the supervisor issues a corresponding operational mode to the drone's and the ground station's controllers, which in turn feature a hierarchical topology. In the next sections, we describe each one of the involved control functions. We assume that the full state of the drone and of the ground station is available: this is reasonable considering that each state variable is measured with redundant sensors, and filtering algorithms are in place as well to reduce the effects of noise.

5.1. Drone controller

For the sake of drone control design, it is useful to distinguish the following three working conditions:

1. Hovering: the drone is kept airborne by the propellers in multi-copter configuration;

2. Dynamic flight with slack tether (free-flight): the drone flies as a conventional aircraft, the front airspeed required to remain airborne is produced by wind and/or by the propellers' thrust. The tether is slack, so it affects the drone dynamics only with its weight and drag;

3. Dynamic flight with taut tether (taut-tether flight): the drone flies as a conventional aircraft, however the tether applies also a pulling force on it.

30

To formulate the feedback control algorithms in an intuitive way, we resorted to three definitions of Euler angles, one for each working condition, expressed as functions of the entries of the rotation matrix H_{BF} (14):

1. Euler angles for hovering $(\varphi_h, \theta_h, \psi_h)$, defined as $Z - Y - X$ right handed rotation sequence from the inertial frame F to body frame B:

$$\begin{bmatrix} \varphi_h \\ \theta_h \\ \psi_h \end{bmatrix} = \begin{bmatrix} \arctan2(H_{BF}(2,3), H_{BF}(3,3)) \\ \arcsin(-H_{BF}(1,3)) \\ \arctan2(H_{BF}(1,2), H_{BF}(1,1)) \end{bmatrix} \tag{33}$$

These are the typical angles used for multi-copter control.

2. Euler angles for free-flight $(\varphi_f, \theta_f, \psi_f)$, defined as $X - Y - Z$ right handed rotation sequence from F to B:

$$\begin{bmatrix} \varphi_f \\ \theta_f \\ \psi_f \end{bmatrix} = \begin{bmatrix} \arctan2(H_{BF}(3,2), H_{BF}(3,1)) \\ \arcsin(-H_{BF}(3,3)) \\ \arctan2(H_{BF}(2,3), H_{BF}(1,3)) \end{bmatrix} \tag{34}$$

With this convention, when the drone flies at zero pitch and roll, the $\vec{z}_B$ axis is parallel to the ground and $\vec{x}_B$ axis points up. These angles correspond to the typical ones for airplane control.

3. Euler angles for taut-tether flight $(\varphi_L, \theta_L, \psi_L)$. These are defined similarly to the Euler angles for free-flight mode, but referring to a neutral condition in which the drone $\vec{x}_B$ axis is aligned with the tether, which corresponds to $\varphi_L = \theta_L = 0$. In these conditions, the yaw angle ψ_L can assume any value, depending on the direction the drone is pointing to. In particular, when $\psi_L = 0$ the drone's $\vec{z}_B$ axis is aligned with the local west axis $\vec{L}_W$ (see Figure 11, right):

$$\begin{bmatrix} \varphi_L \\ \theta_L \\ \psi_L \end{bmatrix} = \begin{bmatrix} \arctan(-H_{BL}(1,2), H_{BL}(1,1)) \\ \arcsin(H_{BL}(1,3)) \\ \arctan(-H_{BL}(2,3), H_{BL}(3,3)) \end{bmatrix} \tag{35}$$

where $H_{BL} = H_{FL} \cdot H_{BF}$ is the rotation matrix between body axis and local reference frame. This triplet is very useful to design the control
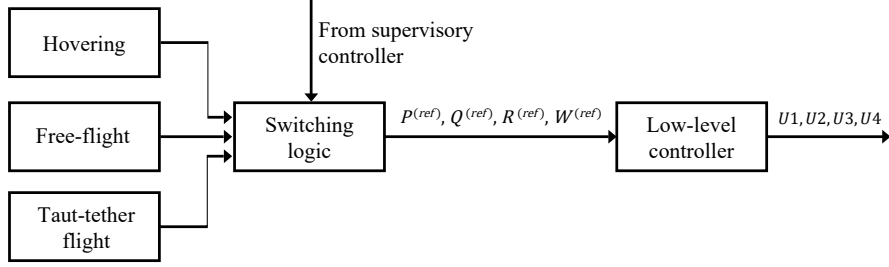
31

Figure 15: Layout of the drone controller. The hovering, free-flight and taut-tether controllers compute reference angular rates $P^{(ref)}$, $Q^{(ref)}$, $R^{(ref)}$ and velocity $W^{(ref)}$ according to their design and possibly based on the inputs sent by the supervisory controller, which is also in charge of the switching logic (see Section 5.3). A unique low-level controller computes the control inputs in order to track the provided references $P^{(ref)}$, $Q^{(ref)}$, $R^{(ref)}$, $W^{(ref)}$.

strategy for taut-tether flight, since the yaw angle is directly linked to the course of the drone (assuming small side-slip angle), which can be feedback-controlled and its reference can be computed by a navigation strategy to achieve, e.g., way-point tracking or path following.

The use of two different sets of Euler angles for hovering and free-flight ((33) and (34), respectively) also allows us to avoid the well-known gimbal lock problem, occurring at pitch angle $\theta = \frac{\pi}{2}$. Indeed, such a pitch value can occur in either one of the two Euler triplets 1. and 2., but never in both triplets at the same time. The Euler angles for tethered flight mode (35) are further introduced in order to describe in an intuitive way the misalignment of the drone's $\vec{x}_B$ axis with respect to the tether, hence simplifying the design of the attitude controllers.

The drone controller consists of a hierarchical structure shown in Figure 15, with a common low-level controller for angular rates and thrust, and different mid- and high-level controllers for the various working conditions. These controllers send to the low-level one suitable reference values of rotational speeds $P^{(ref)}$, $Q^{(ref)}$, $R^{(ref)}$ and of velocity along the $\vec{z}_B$ axis, $W^{(ref)}$. In Section 5.1.1 we recall the low-level attitude controller and the high-level ones for hovering and free-flight, already presented in [23], while in Section 5.1.2 we introduce the

32

one for taut-tether flight.

5.1.1. Low level attitude controller, and hovering and free-flight controllers

The low level controller is the one described in [23]. It is based on simplified equations of the rotational motion and takes into account the non-symmetrical inertia matrix.

The hovering controller computes the reference rotation rates sent to the attitude controller when the drone is in hovering condition. This controller is based again on a hierarchical approach: the inner loop tracks the reference attitude and altitude, a mid level controller tracks the reference speed in $\vec{x}_F$ and $\vec{y}_F$, and an outer loop tracks the position of the drone in the $(\vec{x}_F, \vec{y}_F)$ plane.

The controller for free-flight features a hierarchical logic, with an inner loop responsible for attitude tracking, a middle loop responsible for altitude tracking, and an outer loop for inertial navigation planning. This controller is designed using the Euler angles for free-flight, $(\varphi_f, \theta_f, \psi_f)$. As anticipated in Section 3.3, the steering mechanism exploits a yaw motion instead of a roll one. For further information on these controllers we refer the reader to [23].

5.1.2. Taut-tether flight controller

This controller exploits the Euler angles for taut-tether flight, which define the rotation from the body reference frame B to the local reference frame L. The main difference between taut-tether control and free-flight is that we now provide switching target points in spherical coordinates, following an established approach to obtain figures of eight, see e.g. [32, 12]. Assuming that the tether has instantaneously constant length, the drone is restricted to move along a spherical surface. As a consequence, any motion direction is identified by one planar angle, called velocity angle, see e.g. [32]. This is defined as:

$$\nu = \arctan2\left(-\vec{p}_{(L)}^{T} \vec{L}_W, \ -\vec{p}_{(L)}^{T} \vec{L}_N\right). \tag{36}$$

The reference velocity angle $\nu^{(ref)}$ is computed in order to make the drone move towards the current target point:

$$\nu^{(ref)} = \arctan2 \left((\varphi_{az}^{(ref)} - \varphi_{az}) \cos(\theta_{el}), -(\theta_{el}^{(ref)} - \theta_{el}) \right) \tag{37}$$

where $\theta_{el}^{(ref)}$, $\varphi_{az}^{(ref)}$ are, respectively, the elevation and azimuth angles of the target point. Note that, differently from [32], here the velocity angle is zero when the drone's velocity points towards the ground. This choice allows the controller to carry out figures of eights with "downloops", i.e. moving towards the ground in the outer parts of the eight-figure, and upwards in the middle, which yields a smaller variability of the power output in the traction phase [12]. Then, we design a feedback controller to maintain the θ_L and φ_L angles equal to zero, so to keep a stable tethered flight, and to regulate the yaw ψ_L to make the drone track the reference velocity angle $\nu^{(ref)}$. Specifically, the controller takes the form:

$$\begin{bmatrix} \dot{\varphi}_L^{(ref)} \\ \dot{\theta}_L^{(ref)} \\ \dot{\psi}_L^{(ref)} \end{bmatrix} = \begin{bmatrix} k_{\varphi_L} & 0 & 0 \\ 0 & k_{\theta_L} & 0 \\ 0 & 0 & k_{\psi_L} \end{bmatrix} \begin{bmatrix} 0 - \varphi_L \\ 0 - \theta_L \\ \nu^{(ref)} - \nu \end{bmatrix} \tag{38}$$

Note that the velocity angle is used, instead of the true heading angle ψ_L, to track speed direction more precisely, as it compensates the side slip angle β. Finally, the reference angular velocities around each axis, provided as reference signals to the low-level attitude controller (see Figure 15) are computed by means of the following rotation matrix:

$$\begin{bmatrix} P^{(ref)} \\ Q^{(ref)} \\ R^{(ref)} \end{bmatrix} = \begin{bmatrix} 0 & \sin(\varphi_L) & \cos(\varphi_L)\cos(\theta_L) \\ 0 & \cos(\varphi_L) & -\sin(\varphi_L)\cos(\theta_L) \\ 1 & 0 & \sin(\theta_L) \end{bmatrix} \begin{bmatrix} \dot{\varphi}_L^{(ref)} \\ \dot{\theta}_L^{(ref)} \\ \dot{\psi}_L^{(ref)} \end{bmatrix} \tag{39}$$

Regarding the speed reference $W^{(ref)}$, this is set at a value that is slightly larger than the stall speed of the drone: in this way, if the latter flies faster than $W^{(ref)}$ (thanks to the crosswind effect) the propellers will automatically switch off, while if for any reason (e.g. insufficient wind speed) the drone's velocity component W (i.e., along $\vec{z}_B$ direction in body frame) drops below the

34

reference, the low level controller will engage the propellers and avoid a stall condition.

5.2. Ground station control

The ground station must control the tether reeling speed and/or the applied force by means of the electric motor. We distinguish three possible working conditions:

1. Low tether force: the pulling force is small and the tether is slack. This situation occurs during hovering and in the retraction phase with free-flight reentry strategy. In this working condition, the ground station must keep a low pulling force while avoiding unnecessary reel-out of the tether, which can likely lead to tether entanglement;

2. Generation phase: the tether speed is positive under significant pulling force. This is the working condition in the traction phase of the pumping cycle;

3. Retraction phase with taut tether: there is a non-negligible pulling force applied to the tether, and negative release speed. This working condition occurs during the retraction when the chosen reentry strategy is either the climb and descend one, or the rotation around the ground station.

We developed three controllers to operate in these different working conditions. In all cases, suitable saturations to the commanded torque are included, in order to avoid excessive force peaks on the tether. We denote with $\bar{T}$ the maximum torque, which we choose as a constant value in this work. If needed, one can easily set a torque saturation that depends on other variables, such as the winch speed.

5.2.1. Low tether force

The controller in low force operation requires an accurate position measurement of the drone in order to guarantee that the tether length is larger than the distance between the drone and the ground station, however without exceeding too much, to avoid possible tether entanglement on ground. The idea is to keep

35

an extra-length of the released tether with respect to the drone-ground station distance, by means of a constant offset $\widehat{\Delta L}$. For this kind of control, we used a PD controller tuned on the systems parameters, whose transfer function reads:

$$T_{NoTension}(s) = (K_p + \frac{K_d s}{1 + \frac{K_d}{N_d}s})(L_t^{(ref)} - L_t) \tag{40}$$

where s is the Laplace variable, and K_p, K_d and N_d are tuning parameters based on the model equation (31). The reference tether length $L_t^{(ref)}$ is computed from the drone's position $|\vec{p}_F|$ and the tuning parameter $\widehat{\Delta L}$:

$$L_t^{(ref)} = d + \widehat{\Delta L}. \tag{41}$$

$\widehat{\Delta L}$ is usually chosen as a few meters (see Section 6 for the specific value used in our simulations), depending on the precision of the GPS measure. To avoid tether entanglement, this controller is active only when the tether has to be reeled-in, i.e., during free-flight reentry phases and landing phases. An additional possibility to limit the tether force is the use of a mass-spring-damper system and a feedback controller that reacts on the basis of the spring compression, see [36, 20] for an example.

5.2.2. Generation phase

During the generation phase, the ground station controller must regulate the tether tension to maximize the generated power. To this end, it can be demonstrated (see, e.g., [13]) that the feedback control law that achieves maximum power generation (considering only the traction phase) takes the form:

$$T_{generation} = k_{generation} \dot{\lambda}^2 \tag{42}$$

with

$$k_{generation} = 2\rho \left(S_{up} + S_{down} \right) \bar{C}_L r_w^2 \bar{E} \tag{43}$$

where ρ is the air density and $\bar{C}_L$ and $\bar{E}$ are, respectively, the nominal (i.e., expected by design during the traction phase) lift coefficient and aerodynamic efficiency of the drone.

36

5.2.3. Retraction phase with taut tether

During the retraction phase with taut tether, the ground station controller shall guarantee that the tether is reeled-in under large-enough pulling force. The tether force-speed combination has an impact on the overall efficiency of the pumping cycle. A practical solution is to employ a speed controller with a reference reeling speed that has to be tuned to obtain a good cycle efficiency (see Section 2.2.1). Such a controller is:

$$T_{reentry} = -k_{reentry}(\dot{L}_t^{(ref)} - \dot{L}_t) \tag{44}$$

where the reel-in tether speed reference $\dot{L}_t^{(ref)} < 0$ is usually set at few meters per second. In this work we used a constant gain $k_{reentry}$ tuned by trial and error: the optimization of the reel-in control strategy is currently a topic of research (see Section 7).

5.3. Supervisory controller and transition management

Coordination between ground station and drone controllers is crucial to achieve an efficient and safe operation of the system. The supervisory logic depicted in Figure 14 is responsible for the selection of the mid-level controllers used during the different phases and issues suitable reference signals to such controllers. According to the system's operating principle, we identified five operational phases, see Figure 16, and suitable switching conditions among them, as detailed below. We introduce here the reference signals and the switching conditions employed in each phase in abstract terms: the actual numerical values used in our simulations are reported in Section 6.

1. Hovering to the area where power generation starts (for take-off) and back to the ground station (for landing). In this condition, the hovering controller is active on the drone, and the ground station is controlled in order to have no tension on the tether. During take-off, the hovering controller is commanded to move to a designated position $\vec{p}_{(F),TO}^{(ref)}$, which is sufficiently far from the ground station in downwind direction, to start

pumping operation. The switching between hovering and transition to taut-tether flight occurs when the following condition is met:

$$\|\vec{p}_{(F),TO}^{(ref)} - \vec{p}_{(F)}\|_2 \leq \bar{d}_H \tag{45}$$

where the distance $\bar{d}_H$ is a tuning parameter defining how close the drone shall be to the target when the switching occurs.

During landing, the hovering controller is commanded to move to the ground station.

2. Transition from hovering to traction phase. In this phase, which occurs between take-off and power generation, a chosen reference speed $W^{(ref)}$ along the $\vec{z}_B$ axis and a reference pitch angle $\theta_h^{(ref)}$ are provided to the hovering and low-level controllers on the drone in order to make it steer into crosswind flight. These references are chosen to increase the speed perpendicular to the tether and to enter crosswind flight. Regarding the ground station, in this phase the power generation controller is engaged. The switch to the subsequent traction phase occurs when the following condition is met:

$$W \geq \widehat{W} \tag{46}$$

where $\widehat{W}$ is a speed threshold defined by the user. A sensible choice is to set $\widehat{W}$ equal to the stall speed of the aircraft plus a reasonable margin (e.g., +10%).

3. Traction phase. The controller for taut-tether flight is enabled on the drone, which starts to track reference points in the elevation-azimuth plane in order to carry out figure-of-eight crosswind trajectories. The two employed reference points feature the same elevation $\theta_{el}^{(ref)}$ and azimuth angles φ_{az}^{TR+} and φ_{az}^{TR-}. The current reference azimuth $\varphi_{az}^{(ref)}$ (see Section 5.1.2) is set by the supervisory controller to either φ_{az}^{TR+} or φ_{az}^{TR-} according to a switching strategy based on a suitable proximity condition, see e.g. [32], [12]. During the traction phase, the ground station control is set to power generation. Switching to the retraction phase is commanded

38

when the tether length exceeds a set threshold and, at the same time, the drone velocity vector has a component pointing upwards:

$$L_t \geq L_{max} \wedge \dot{p}_{\vec{z}_F} > 0 \tag{47}$$

This condition ensures that the retraction phase does not begin when the drone moves towards the ground, making the maneuver safer.

4. Retraction phase. The employed low-level controllers, reference variables and switching conditions of the retraction phase depend on the chosen reentry strategy:

- For the free-flight reentry, the employed controllers are the free-flight one for the drone, and the low force one for the ground station. The supervisory controller sends to the drone a target position $\vec{p}_{(F),RE}^{(ref)}$, which is a design parameter. In particular, the $\vec{x}_F$ and $\vec{z}_F$ components of $\vec{p}_{(F),RE}^{(ref)}$ are set at a desired distance and altitude in downwind direction with respect to the ground station, while the $\vec{y}_F$ component features a chosen magnitude and its sign is the same as that of the drone velocity component $\dot{p}_{\vec{y}_F}$ at the end of the traction phase. The switch to the traction phase (for the next pumping cycle) is commanded when the tether length falls below a set lower threshold $\underline{L}_t$:

$$L_t \leq \underline{L}_t. \tag{48}$$

- For the rotation around the ground station, the taut-tether flight controller is kept engaged, and it is given a reference elevation $\theta_{el}^{(ref)} = \theta_{el}^{rot}$ and azimuth $\varphi_{az}^{(ref)} = \pm \pi$, where the positive value (i.e., π) is chosen if the drone velocity component $\dot{p}_{\vec{y}_F}$ is positive, while the negative one is used if $\dot{p}_{\vec{y}_F} < 0$. In this way, the drone continues to fly in the same direction (respectively towards left - $\dot{p}_{\vec{y}_F} > 0$ - or right - $\dot{p}_{\vec{y}_F} < 0$ - looking at the drone from the ground station) to carry out the rotation. The ground control operational mode is set to retraction phase with taut tether (see Section 5.2.3) only when the drone

39

reaches a position such that $|\theta_{el}| \geq \pi/4$. When the position component $p_{\vec{x}_F}$ of the drone switches from negative to positive (i.e. when the drone has completed a rotation spanning the whole half-plane "behind" the ground station), the switch to the next traction phase is commanded.

- For the climb and descend reentry maneuver, the taut-tether flight controller is kept engaged and it is given a reference elevation $\theta_{el}^{(ref)} = \theta_{el}^{CD}$ and azimuth angles φ_{az}^{CD+} and φ_{az}^{CD-}, using the same strategy as in the traction phase. The target points are chosen to make the drone increase the elevation angle, in order to decrease the tether force thanks to a smaller projection of the absolute wind in tether direction. The ground control operational mode is set to retraction phase with taut tether. The switching condition to traction phase is (48).

5. Transition from power generation to hovering. This phase is engaged when the system exits the power generation phase and enters the hovering mode, for example to carry out a landing maneuver (see point 1. above). The ground station controller is set to low force operation. At the same time, the supervisory controller sends to the drone a reference pitch angle (in free-flight convention) $\theta_f^{(ref)} = \pi/2$. In this way, the tether force drops under the action of the ground station controller, and the drone pitches up and gains altitude using the propellers. The switch to hovering phase (described at point 1. above) is commanded when the drone's pitch (in hovering convention) is small enough:

$$|\theta_h| \leq \bar{\theta}_h \tag{49}$$

where the threshold $\bar{\theta}_h$ is a user-defined parameter, to be chosen inside the region of attraction of the hovering controller.

Figure 16 presents the switching conditions among the described phases, while Table 2 summarizes the drone and ground station controllers employed in each phase.

	Phase				
	Hovering	Transition to generation	Pumping (traction)	Pumping (reentry)	Transition to hovering
Drone	HO	HO	TT	TT or FF	FF
Ground s.	LF	GE	GE	TT or LF	LF

Table 2: Active drone and ground station controllers in the different operational phases. Drone controllers: HO=Hovering; FF=Free-flight; TT=Taut tether. Ground station controllers: LF=Low force; GE=Power generation; TT=Taut tether retraction.
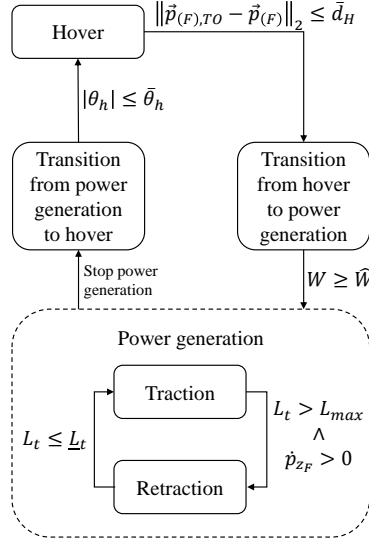

Figure 16: Supervisory control strategy with switching conditions among phases.

6. Simulations results

Several simulations of all-round operation have been performed. The relevant system parameters are shown in Table 3, and the aerodynamic coefficients as a function of α, β are presented in Figure 17.

The low level flight controllers have been designed using either pole placement or LQR techniques, with the tuning parameters reported in Table 4. Regarding the ground station controller, the employed parameters are $K_p = 0.67$, $K_d = 2.7$, $N_d = 20$, $\widehat{\Delta L} = 5\,\mathrm{m}$, $\dot{L}_t^{(ref)} = -3\,\mathrm{m/s}$ and $k_{reentry} = 200$. The winch

Table 3: System parameters used in the simulations.

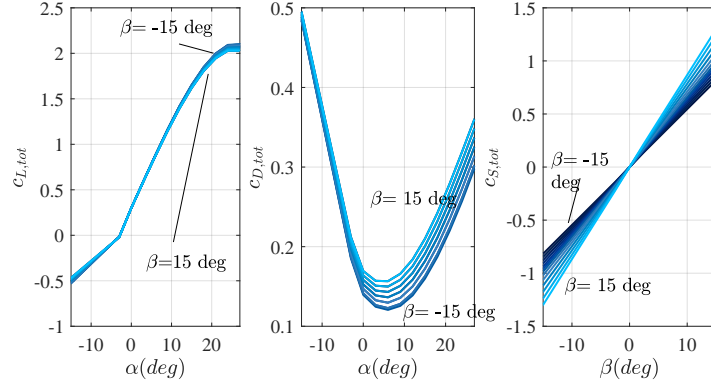| Parameter	Unit	Value
Air density ρ	kg/m^2	1.2
Gravity acceleration g	m/s^2	9.81
Drone		
Mass m	kg	11.3
Inertia matrix I	kg m^2	$\begin{bmatrix} 4.53 & 0 & -1.35 \\ 0 & 3.28 & 0 \\ -1.35 & 0 & 5.49 \end{bmatrix}$
Total effective surface area S	m^2	0.21
Tether connection point $\vec{p}_{t(B)}$	m	$\begin{bmatrix} -1 & 0 & 0 \end{bmatrix}^T$
Max prop. speed	rpm	12000
Thrust coefficient b_j	N/rpm^2	1.1e-6
Drag coefficient c_j	N/rpm^2	2.04e-8
Prop. distance $d_{\vec{x}_B i}$, $d_{\vec{y}_B i}$	m	$\begin{bmatrix} 0.632 & 0.395 \\ 0.632 & 0.585 \\ 0.632 & 0.395 \\ 0.632 & 0.585 \end{bmatrix}$
Tether		
Maximum length	m	500
Diameter d_t	mm	0.83
Max elongation ϵ_{max}	%	1
Drag coefficient $c_{D,t}$	-	1
Minimum breaking load	N	1600
Winch		
Radius r_w	m	0.159
Moment of inertia J	kg m^2	0.2
Friction coefficient β_f	Nm s	0.01

Figure 17: Aerodynamic coefficients used in the simulations. Lift and drag coefficients are plotted as function of angle of attack and for different side slip angle values, while the side force coefficient is plotted as a function of side slip angle and for different values of angle of attack. Coefficients obtained by computing the aerodynamic forces with CFD analysis using the software SU2 [34] and then dividing the force by the term $\frac{1}{2}\rho S v_a^2$, see (21).

torque saturation is set at $\bar{T} = 160\,\mathrm{Nm}$, corresponding to a tether force of about 1000 N).The computed value of $k_{generation}$ (see (42)-(43)) is 0.5324. Finally, the numerical values of the parameters pertaining to the supervisory controller, described in Section 5.3, are reported in Table 5.

In the simulation analyzed here, the wind velocity $\vec{v}_{w(F)}$ has been computed as a vector with average value of 7 m/s along the inertial $\vec{x}_F$ axis, and zero-mean uniformly distributed random perturbations on all components.

Figure 18 shows the path performed by the drone: after the first hovering phase, two pumping cycles with free-flight reentry are carried out, before transitioning again to hovering and then landing. As described in the previous sections, the drone is commanded to take-off from the ground station in hovering mode until it reaches the point chosen to start the power generation. Then, transition from hovering to tethered flight starts: the drone rapidly increases its speed component W, while the ground station engages the generation phase controller. When the front speed exceeds the threshold $\widehat{W}$, the taut-tether flight controller is enabled and the drone starts the generation phase, tracking figure-of-eight paths. When the length of the tether reaches the value L_{max}, the retraction

43

Table 4: Control design techniques and tuning parameters employed for the mid- and low-level loops. PP: Pole Placement; LQR: Linear-Quadratic Regulator. The design parameters are the closed loop poles for PP and the Q, R matrices for LQR.

Control loop	Design parameters
Low level - [23] eq. (10)-(12)	
Angular rates (PP)	40 rad/s
Velocity component W (PP)	20 rad/s
Hovering - [23] eq. (13)-(19)	
Attitude (PP)	5 rad/s
Velocity (PP)	1 rad/s
Position (PP)	0.2 rad/s
Free Flight - [23] eq. (20)-(23)	
Attitude (PP)	10 rad/s
Altitude and vertical speed (LQR)	$Q = \begin{bmatrix} 100 & 0 \\ 0 & 1 \end{bmatrix}$ $R = \begin{bmatrix} 1000 & 0 \\ 0 & 100 \end{bmatrix}$
Taut-tether flight - Section 5.1.2	
Attitude (PP)	5 rad/s

Table 5: Supervisory controller: values of the parameters introduced in Section 5.3 employed in the simulations.

Parameter	Unit	Value
Hovering		
$\bar{p}^{(ref)}_{(F),TO}$	m	$\begin{bmatrix} 80 & 0 & 20 \end{bmatrix}^T$
$\bar{d}_H$	m	5
Transition to power generation		
$W^{(ref)}$	m/s	25
$\theta^{(ref)}_h$	rad	0
$\widehat{W}$	m/s	22
Traction phase		
$\theta^{(ref)}_{el}$	rad	0.6
$\varphi^{TR+}_{az}, \varphi^{TR-}_{az}$	rad	± 0.7
L_{max}	m	180
Retraction phase		
$\bar{p}^{(ref)}_{(F),RE}$	m	$\begin{bmatrix} 120 & \pm 40 & 40 \end{bmatrix}^T$
θ^{rot}_{el}	rad	1.1
θ^{CD}_{el}	rad	1.2
$\varphi^{CD+}_{az}, \varphi^{CD-}_{az}$	rad	± 1.1
$\underline{L}_t$	m	135
Transition to hovering		
$\bar{\theta}_h$	rad	$\pi/3$

45

phase begins. We comment next the behavior when a free-flight reentry is implemented, since it proved to be the most efficient strategy. In Section 6.1, we compare this approach with the other two alternatives described in Section 2.2.1. When the reentry phase is concluded (the tether length falls below $\underline{L_t}$), another pumping cycle starts. Figure 3 shows the same path in terms of spherical coordinates. It can be seen that the azimuth angle is kept between ± 40 degrees, and that the elevation angle during the traction phase is between 30 and 15 degrees. Figure 19 presents the tether force, speed, and mechanical power during a simulation encompassing take-off, three pumping cycles, and landing. It is clearly visible how the free-flight strategy is able to quickly reduce the tether force during the retraction. The tether force has a variation of more than 200 N during the power generation phase with a mean value around 500 N, and the tether is released at around 2 m/s. This is consistent with the chosen reel-out strategy: in fact, considering 7 m/s average wind speed and an elevation angle θ_{el} of about 22 degrees, the wind speed in tether direction results to be around 6.5 m/s, and 1/3 of it corresponds to 2.15 m/s. The mean power generated during 2 cycles is 751 W, while considering only the traction phase the mean power generated is about 908.6 W. The Euler angles in the three adopted conventions (hovering, free-flight, and taut-tether flight) during a simulation comprising the take-off and one pumping cycle are shown in Figure 20. The white sections denote the engaged flight controller: the hovering one until about 35 s, then the taut-tether one, finally the free-flight one for the reentry, at about 76 s. The switching behavior of the target-point strategy in the traction phase is clearly visible, with the yaw angle ψ_L transitioning from a few degrees (i.e., moving towards the local West) to about $-\pi$ (i.e., moving towards the local East). Still regarding the taut-tether flight, Figure 21 shows the course of the velocity angle and its reference. Finally, Figure 22 presents the low-level control inputs U_1, U_2, U_3, and U_4 during take-off, three pumping cycles, and landing. It can be noted that the propellers switch on ($U_1 \neq 0$) also during the traction phase, when the apparent speed is not large enough: this is due to the fact that the tested wind speed of 7 m/s is close to the minimum one at which the
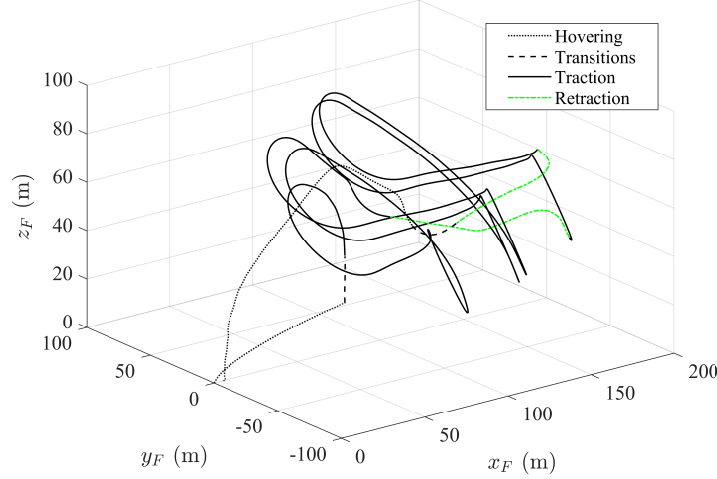
46

Figure 18: Pumping operation with free-flight reentry: 3D drone path including take-off, hovering, transition to power generation, two pumping cycles, transition to hovering, and landing.

system can remain airborne. The same figure also shows how the moment U_3 has non-zero average during crosswind flight, i.e. active control must be used to keep the drone's pitch angle at the desired reference. This behavior can be improved, e.g., by moving the tether attachment point in the $\vec{z}_B$ direction or changing the trim of the wings.

6.1. Comparison among reentry strategies

We compared the three reentry phase strategies introduced in Section 2.2.1 in simulation, in order to study the advantages and drawbacks of each one. From the point of view of implementation, the simplest strategies are those with taut tether, because they avoid transitions between taut and slack tether, decreasing the number of involved controllers and the complexity of coordinating them. Figure 4 shows the trajectory with the reentry strategy consisting of a complete rotation around the ground station. In the first part of the reentry phase, the apparent wind is very high, because the drone is flying in downwind position, while when the drone moves upwind with respect to the ground station the
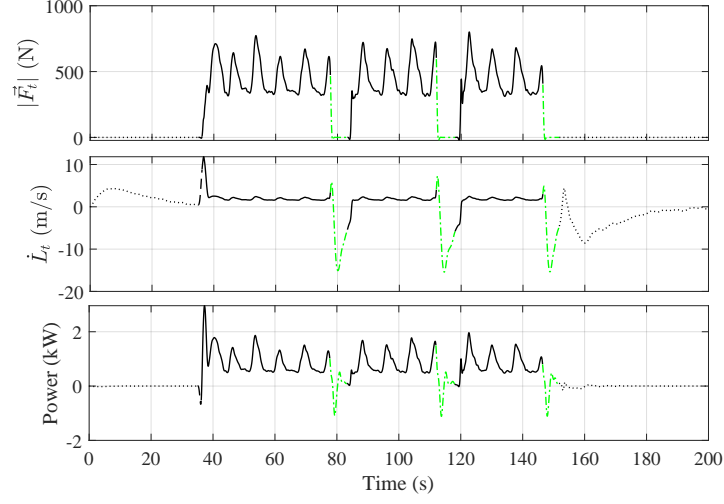
47

Figure 19: Pumping operation with free-flight reentry: ground station variables during take-off, three pumping cycles, and landing. From top: tether force, tether speed, and mechanical power. Dotted line: hovering; dashed: transitions; solid: traction phase; green dash-dotted: retraction phase.
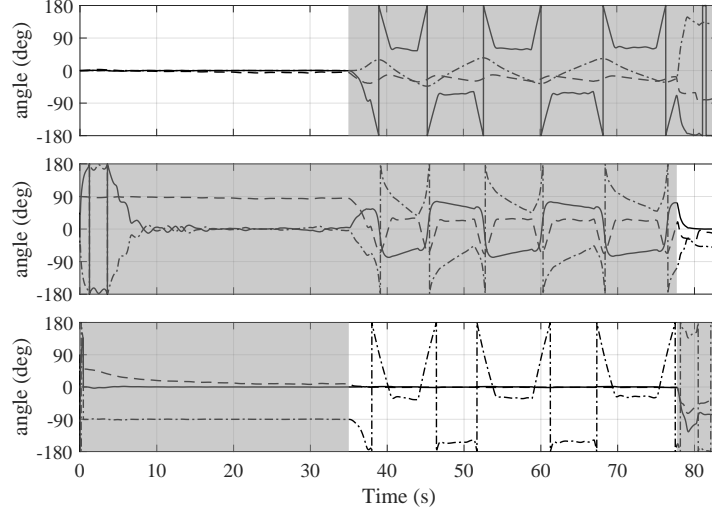

Figure 20: Simulation results: attitude of the drone during take-off and one pumping cycle. From top to bottom: Euler angles for hovering, Euler angles for free flight, and Euler angles for taut-tether flight. Solid lines: roll angle (φ_h, φ_f, φ_L); Dashed lines: pitch angle (θ_h, θ_f, θ_L); Dash-dotted lines: yaw angle (ψ_h, ψ_f, ψ_L). White sections of the plots indicate the engaged flight controller (from top to bottom: hovering, free-flight, and taut-tether flight).
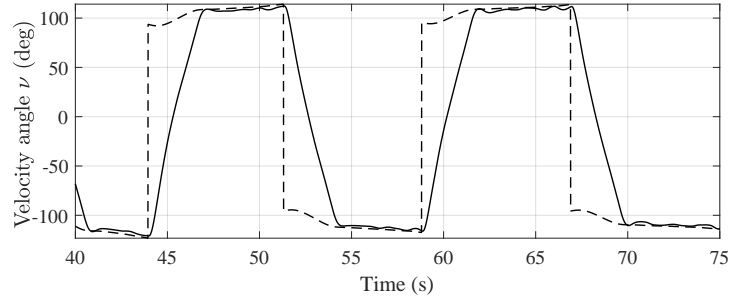
48

Figure 21: Simulation results. Traction phase: velocity angle (solid) and its reference (dashed) during two figure-of-eight paths.
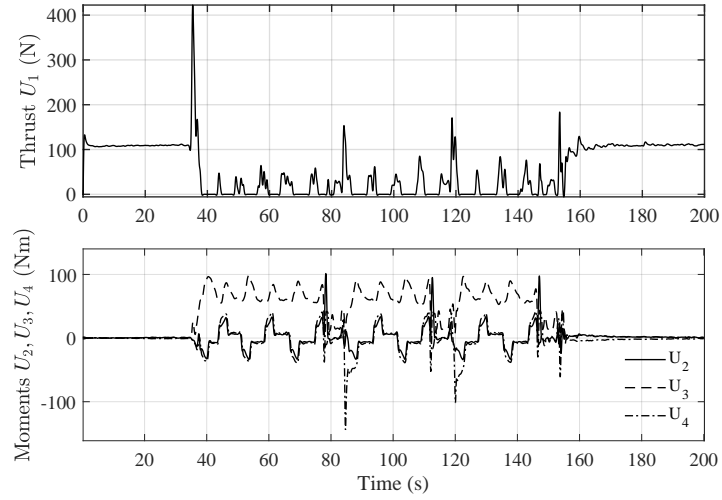

Figure 22: Simulation results, course of the total thrust U_1 (upper plot), and moments U_2 (lower plot, solid line), U_3 (dashed), and U_4 (dash-dotted) during take-off, three pumping cycles, and landing.

49

apparent wind is very low, and the tether force decreases substantially. Figure 5 shows the trajectory in terms of azimuth and elevation angles for the climb and descend reentry strategy. The drone continues to perform figure-of-eight paths but at higher elevation angle, above 60 degrees, thus reducing the apparent wind seen by the tether. In this way, the tether can be reeled in under relatively lower force.

We compared the three strategies in terms of cycle efficiency, defined as:

$$
\eta = \frac{(t_{ce} - t_{cs}) \int\limits_{t_{ts}}^{t_{te}} P(\tau)d\tau}{(t_{te} - t_{ts}) \int\limits_{t_{cs}}^{t_{ce}} P(\tau)d\tau}, \tag{50}
$$

where $P = |\vec{F}_t|\dot{L}_t$ is the mechanical power t_{cs}, t_{ce} are the start and end time of the pumping cycle, and t_{ts}, t_{te} the start and end time of the traction phase only. In other words, η is the ratio between the so called cycle power (average power of the pumping cycle) and the average power during traction only. It is a good metric to evaluate the impact of the retraction phase, also accounting for the duty cycle. The results are reported in Figure 23. The best reentry strategy in terms of efficiency is clearly the free-flight one, because it is fast and requires very low power during retraction, scoring an efficiency of about 83%. Regarding the strategies with taut tether, it turns out that the complete rotation around the ground station has a higher efficiency (about 46%) than the climb and descend strategy. This is due to the fact that it requires less power to pull the tether when the drone is in the upwind zone. The climb and descend reentry strategy has the lowest efficiency (40%) among the three, however the average cycle power is still positive.

Figure 24 shows a comparison among the three strategies in terms of tether force and length in a simulation encompassing take-off and at least two pumping cycles for each one. It can be noted that both the duty cycle and the tether force during retraction are significantly better in the free-flight approach. The rotation around the ground station gives rise to a longer traction phase, because the tether reels out also in the first part of the rotation, until the drone reaches
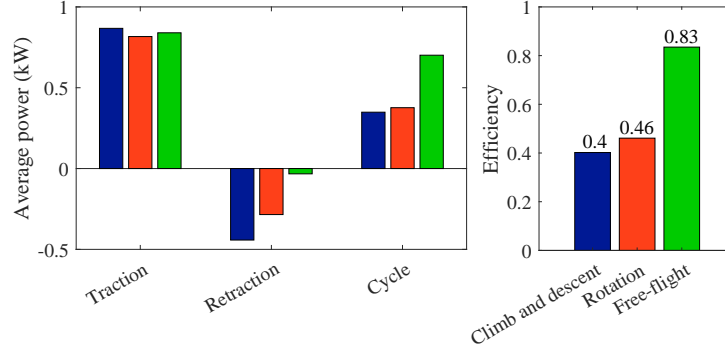
50

Figure 23: Simulation results. Comparison among reentry strategies. Left: average power during the traction phase, the retraction phase, and the whole pumping cycle power, for the free-flight strategy (blue), the rotation around ground station (red), and the climb and descend (green). Right: cycle efficiency.

$|\theta_{el}| \geq \pi/4$. This behavior results in a longer cycle. Note that both the climb and descend strategy and the rotation around the ground station still feature a rather high tether force during the retraction phase.

7. Conclusions and suggested next steps

The models and controllers described in this work form a complete simulation suite that can be implemented in numerical ODE solvers to evaluate the system behavior and to support experimental testing and product development for VTOL pumping AWE systems in all operating conditions. Through this model, a comparison between different reentry strategies has been carried out. The results confirm that the reentry strategy in free flight is the best solution in terms of cycle efficiency, which is roughly twice that of the other considered approaches. Moreover, a steering authority analysis has been presented, providing results that link drone design parameters to its maneuverability during taut-tether flight.

One of the main limitations of the presented work is the lack of a robustness analysis with different and time-varying wind speed profiles, both in terms of
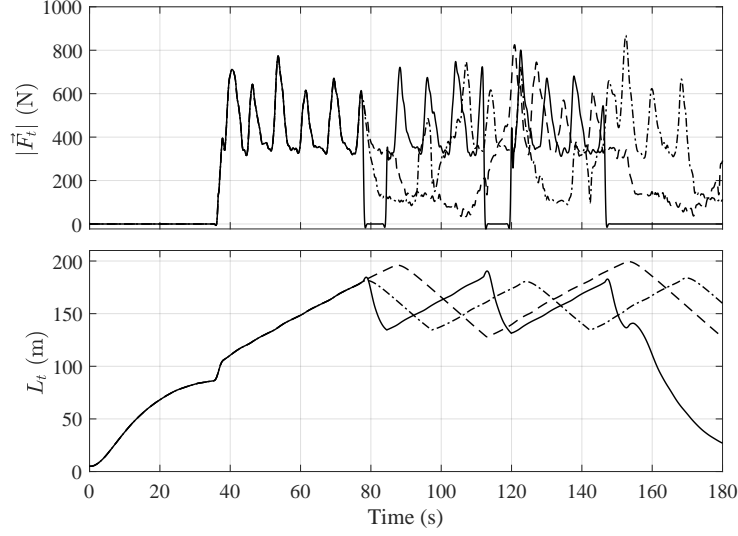
51

Figure 24: Simulation results. Course of tether force and length with the three different reentry strategies: free-flight (solid), rotation around the ground station (dashed), and climb and descend (dash-dotted). The take-off and first traction phase are the same in the three simulations. For the free-flight strategy, a landing maneuver is carried out after three cycles.

speed and direction. This analysis would require a realistic model of the wind field, and its outcome may indicate that robust automation strategies are needed to cope with wind variability and/or sudden events, like wind gusts. The development of such robust approaches is an important direction for further research and also presents interesting methodological challenges, given the system nonlinearities and the need to design a distributed control approach. Moreover, in our hierarchical control system several tuning parameters are present, which we set by trial and error: another interesting topic is to devise optimal tuning methods for these parameters. In addition to these research directions, other suggested next steps are the inclusion of a multi-body tether model, to improve the model accuracy, and the experimental test of the approach on a real prototype, in order to validate the results and improve the simulation environment.

52

References

[1] A. Cherubini, A. Papini, R. Vertechy, and M. Fontana, "Airborne wind energy systems: A review of the technologies," *Renewable and Sustainable Energy Reviews*, vol. 51, pp. 1461–1476, 2015.

[2] R. Schmehl, Ed., *Airborne Wind Energy - Advances in Technology Development and Research.* Singapore: Springer, 2018.

[3] International Renewable Energy Agency (IRENA), Abu Dhabi, "Innovation Outlook: Off-shore Wind". accessed on 17/1/2019. [Online]. Available: https://www.irena.org/publications/2016/Oct/ Innovation-Outlook-Offshore-Wind

[4] European Commission - Directorate-General for Research and Innovation, "Study on Challenges in the Commercialisation of Airborne Wind Energy Systems", September 2018. Last accessed: 17/1/2019. [Online]. Available: https://op.europa.eu/en/ publication-detail/-/publication/a874f843-c137-11e8-9893-01aa75ed71a1/ language-en/format-PDF/source-112940934

[5] S. W. et al., "Future emerging technologies in the wind power sector: A European perspective," *Renewable and Sustainable Energy Reviews*, vol. 113, p. 109270, 2019. [Online]. Available: http: //www.sciencedirect.com/science/article/pii/S1364032119304782

[6] L. Fagiano, M. Milanese, and D. Piga, "High-altitude wind power generation," *IEEE Transactions on Energy Conversion*, vol. 25, no. 1, pp. 168 –180, mar. 2010.

[7] C. L. Archer and K. Caldeira, "Global assessment of high-altitude wind power," *Energies*, vol. 2, no. 2, pp. 307–319, 2009.

[8] C. L. Archer, L. D. Monache, and D. L. Rife, "Airborne wind energy: Optimal locations and variability," *Renewable Energy*, vol. 64, pp. 180– 186, 2014.

[9] P. Bechtle, M. Schelbergen, R. Schmehl, U. Zillmann, and S. Watson, "Airborne wind energy resource analysis," *Renewable Energy*, vol. 141, pp. 1103 – 1116, 2019.

[10] D. Vander Lind, "Analysis and flight test validation of high performance airborne wind turbines," in *Airborne Wind Energy*. Berlin Heidelberg: Springer, 2013, ch. 28, pp. 473–490.

[11] F. Bauer, R. M. Kennel, C. M. Hackl, F. Campagnolo, M. Patt, and R. Schmehl, "Drag power kite with very high lift coefficient," *Renewable Energy*, vol. 118, pp. 290 – 305, 2018. [Online]. Available: http://www.sciencedirect.com/science/article/pii/S0960148117310285

[12] M. Erhard and H. Strauch, "Flight control of tethered kites in autonomous pumping cycles for airborne wind energy," *Control Engineering Practice*, vol. 40, pp. 13–26, 2015.

[13] A. Zgraggen, L. Fagiano, and M. Morari, "Automatic retraction and full-cycle operation for a class of airborne wind energy generators," *IEEE Transactions on Control Systems Technology*, vol. 24, no. 2, pp. 594–698, 2016.

[14] G. Licitra, A. Bürger, P. Williams, R. Ruiterkamp, and M. Diehl, "Optimal input design for autonomous aircraft," *Control Engineering Practice*, vol. 77, pp. 15 – 27, 2018.

[15] G. Licitra, J. Koenemann, A. Bürger, P. Williams, R. Ruiterkamp, and M. Diehl, "Performance assessment of a rigid wing Airborne Wind Energy pumping system," *Energy*, vol. 173, no. C, pp. 569–585, 2019. [Online]. Available: https://ideas.repec.org/a/eee/energy/v173y2019icp569-585.html

[16] U. Fechner, R. van der Vlugt, E. Schreuder, and R. Schmehl, "Dynamic model of a pumping kite power system," *Renewable Energy*, 2015.

[17] J. Heilmann and C. Houle, "Economics of pumping kite generators," in *Airborne Wind Energy*, U. Ahrens, M. Diehl, and R. Schmehl, Eds. Berlin Heidelberg: Springer, 2013, ch. 15, pp. 271–284.

[18] R. Ruiterkamp and S. Sieberling, *Airborne Wind Energy*, ser. Green Energy and Technology. Berlin: Springer-Verlag, 2014, ch. 26. Description and Preliminary Test Results of a Six Degrees of Freedom Rigid Wing Pumping System, p. 443.

[19] J. Stuyts, G. Horn, W. Vandermeulen, J. Driesen, and M. Diehl, "Effect of the electrical energy conversion on optimal cycles for pumping airborne wind energy," *IEEE Transactions on Sustainable Energy*, vol. 6, no. 1, pp. 2–10, 2015.

[20] L. Fagiano, E. Nguyen-Van, F. Rager, S. Schnez, and C. Ohler, "Autonomous Take Off and Flight of a Tethered Aircraft for Airborne Wind Energy," *IEEE Transactions on Control Systems Technology*, vol. 26, no. 1, pp. 151–166, 2018.

[21] K. Vimalakanthan, M. Caboni, J. Schepers, E. Pechenik, and P. Williams, "Aerodynamic analysis of Ampyx's airborne wind energy system," *Journal of Physics: Conference Series*, vol. 1037, p. 062008, jun 2018. [Online]. Available: https://doi.org/10.1088%2F1742-6596%2F1037%2F6%2F062008

[22] R. Luchsinger, D. Aregger, F. B. D. Costa, C. Galliot, F. Gohl, J. Heilmann, H. Hesse, C. Houle, T. A. Wood, and R. S. Smith, *Pumping Cycle Kite Power with Twings, in Schmehl R. (eds). Airborne Wind Energy. Green Energy and Technology.* Singapore: Springer, 2018.

[23] D. Todeschini, L. Fagiano, C. Micheli, and A. Cattano, "Control of vertical take off, dynamic flight and landing of hybrid drones for airborne wind energy systems," in *2019 American Control Conference (ACC)*. IEEE, 2019, pp. 2177–2182.

[24] S. Rapp, R. Schmehl, E. Oland, and T. Haas, "Cascaded pumping cycle control for rigid wing airborne wind energy systems," *Journal of Guidance, Control, and Dynamics*, vol. 42, no. 11, pp. 2456–2473, 2019.

[25] H. Li, D. Olinger, and M. Demetriou, *Attitude Tracking Control of an Airborne Wind Energy System*, ser. Green Energy and Technology. Springer, april 2018, pp. 215–239.

[26] E. Bontekoe, "Up! - how to launch and retrieve a tethered aircraft," Master's thesis, TU Delft, August 2010, accessed in September 2018 at http://repository.tudelft.nl/.

[27] L. Fagiano and S. Schnez, "On the take-off of airborne wind energy systems based on rigid wings," *Renewable Energy*, vol. 107, pp. 473–488, 2015.

[28] Skypull SA. [Online]. Available: https://www.skypull.technology/

[29] M. L. Loyd, "Crosswind kite power," *Journal of Energy*, vol. 4, no. 3, pp. 106–111, 1980.

[30] L. Fagiano and M. Milanese, "Airborne wind energy: an overview," in *American Control Conference 2012*, Montreal, Canada, 2012, pp. 3132–3143.

[31] M. Erhard and H. Strauch, "Control of towing kites for seagoing vessels," *IEEE Transactions on Control Systems Technology*, vol. 21, no. 5, pp. 1629–1640, 2012.

[32] L. Fagiano, A. Zgraggen, M. Morari, and M. Khammash, "Automatic crosswind flight of tethered wings for airborne wind energy: modeling, control design and experimental results," *IEEE Transactions on Control Systems Technology*, vol. 22, no. 4, pp. 1433–1447, 2014.

[33] B. Etkin, *Dynamics of Atmospheric Flight*. Dover, 2005.

[34] T. D. Economon, F. Palacios, S. R. Copeland, T. W. Lukaczyk, and J. J. Alonso, "Su2: An open-source suite for multiphysics simulation and design," *AIAA Journal*, vol. 54, no. 3, pp. 828–846, 2016.

[35] L. Fagiano, "Control of tethered airfoils for high-altitude wind energy generation," Ph.D. dissertation, Politecnico di Torino, 2009. [Online]. Available: http://lorenzofagiano.altervista.org/docs/PhD_thesis_Fagiano_Final.pdf

[36] L. Fagiano, E. Nguyen-Van, F. Rager, S. Schnez, and C. Ohler, "A Small-Scale Prototype to Study the Takeoff of Tethered Rigid Aircrafts for Airborne Wind Energy," *IEEE/ASME Transactions on Mechatronics*, vol. 22, no. 4, pp. 1869–1880, 2017.